Title

High-resolution geophysical and geochronological analysis of a relict shoreface deposit offshore central California: Implications for slip rate along the Hosgri fault

Journal

Geosphere, 19(6)

ISSN

1553-040X

Authors

Kluesner, Jared W

Johnson, Samuel Y

Nishenko, Stuart P

et al.

Publication Date

2023-12-01

DOI

10.1130/ges02657.1

Peer reviewed

High-Resolution Geophysical and Geochronological Analysis of a Relict Shoreface Deposit Offshore Central California: Implications for Slip Rate along the Hosgri Fault

Jared W. Kluesner[1], Samuel Y. Johnson[1], Stuart P. Nishenko[2], Elisa Medri[3], Alexander R. Simms[3], H. Gary Greene[4], Harrison J. Grey[5], Shannon A. Mahan[5], Emma T. Krolczyk[5], Daniel S. Brothers[1], James E. Conrad[1]

[1]U.S. Geological Survey, Pacific Coastal and Marine Science Center, Santa Cruz, CA

[2]Pacific Gas and Electric (retired)

[3]Department of Earth Sciences, University of California Santa Barbara, Santa Barbara, CA

[4]Moss Landing Marine Laboratories, Moss Landing, CA

[5]U.S. Geological Survey, Geosciences and Environmental Change Science Center, Denver, CO, 80225

ABSTRACT

The Cross-Hosgri Slope (CHS) is a bathymetric lineament that crosses the eastern strand of the Hosgri Fault (EHF) offshore Point Estero, central California. Recently collected CHIRP seismic reflection profiles and sediment cores provide the basis for a reassessment of CHS origin and the proposed lateral slip rate of the EHF based on offset of the CHS lower slope break. The CHS is comprised of two distinct stratigraphic units. The lower unit (Unit 1) overlies the post-Last Glacial Maximum transgressive surface of erosion and is interpreted as a Younger Dryas (~12.8 to 11.5 ka) shoreface deposit based on radiocarbon and OSL ages, seismic facies, sediment texture, sediment infauna, and heavy mineral component. The shoreface was abandoned and partly eroded during rapid sea-level rise from about 11.5 to 7 ka. Unit 2 consists of fine sand and silt deposited in a mid-shelf environment when the rate of sea-level rise slowed between ~7 ka and the present. Although Unit 2 provides a thin, relatively uniform cover over the lower slope break of the older shoreface, this feature still provides a valuable piercing point, and the previously estimated EHF slip rate of 2.6 ± 0.9 mm/yr remains valid. Full-waveform processing of CHIRP data resulted in significantly higher resolution in coarser grained strata that are typically difficult to interpret with more traditional envelope processing. Our novel combination of offshore radiocarbon and OSL dating is the first application for offshore paleoseismic studies, and our results indicate the utility of this approach for future marine neotectonic investigations.

INTRODUCTION

Assessment of earthquake hazards requires comprehensive characterization of active faults, including documentation of fault location, length, connectivity, slip rate, and rupture

history. Acquiring such documentation for faults in the near offshore can be especially important given the possible impact on commonly dense coastal population and infrastructure. The target of this paper is the slip rate of one such structure, the Hosgri Fault of central California (Fig. 1). We focus on a distinct, linear, southwest-facing bathymetric slope referred to as the cross-Hosgri slope (CHS; Johnson et al., 2014; Fig. 2). The CHS crosses and is offset by the main strand of the Hosgri Fault about 30 to 35 km north of Point Buchon and the Pacific Gas and Electric (PG&E)-operated Diablo Canyon Nuclear Power Plant.

Using global sea-level curves (Stanford et al., 2011), Johnson et al. (2014) interpreted the CHS as the relict shoreface of a now-eroded latest Pleistocene sand spit that formed during sea-level rise following the Last Glacial Maximum (LGM). The current depth of the CHS shoreface approximately coincides with sea level during a period of relatively slower eustatic rise, the Younger Dryas stadial (~12;800–11;500 yr B.P.), and the CHS was inferred to have been rapidly submerged and preserved during the following period of rapid eustatic rise, from about 11,500 to 7,000 yr B.P. Using high-resolution bathymetry (Fig. 2 inset), Johnson et al. (2014) plotted and analyzed closely spaced (12.5 m) normal-to-slope profiles bracketing the trace of the Hosgri fault where it crosses the lower slope break of the CHS. They documented 30.3 ± 9.4 m (mean and 2 standard deviations) of dextral fault offset and about 70 to 110 cm of vertical offset. They then used the estimated Younger Dryas age of the CHS and the amount of dextral offset to infer a slip rate of 2.6 ± 0.9 mm/yr on the main strand of the Hosgri fault.

Both the depositional model of the CHS and the Hosgri slip rate in Johnson et al. (2014) were derived by correlation with a global sea-level curve. Highest-resolution Compressed High Intensity Radar Pulse (CHIRP) imagery and ground truthing constraints from CHS sediments,

including physical properties, geochronology, and petrology, were lacking. Given the limitations and uncertainty associated with the Johnson et al. (2014) approach, USGS, PG&E, and the University of California at Santa Barbara collaborated through Cooperative Research and Development Agreements on a 2019 geophysical and coring program focused primarily on the CHS. The goals of the program were to better understand CHS stratigraphy and sedimentology, and to provide samples for geochronologic studies. Initial results of this recent work are presented in Medri et al. (2023), who show that the CHS is underlain by distinct, post-LGM, stratigraphic units deposited in environments ranging from shoreface to mid-shelf and ranging in age from about 12,400 yr B.P. to Modern based on radiocarbon dating. Medri et al. (2023) focus on the sedimentology of a middle unit of mid-shelf sediments deposited between about 7,000 and 1,000 yr. B.P., which was interpreted as a subaqueous clinoform built by wave-supported gravity flows. Our paper primarily focuses on the underlying lowest post-LGM stratigraphic unit, which is used for estimating fault slip rate. We supplement the radiocarbon dating of Medri et al. (2023) with new Optically Stimulated Luminescence (OSL) dating of quartz sediment grains to provide further constraints on the geochronology of the CHS. In addition, we use advanced processing techniques on full-waveform CHIRP data to greatly improve the vertical resolution and clarity of the seismic stratigraphy and fault offsets within the coarse grain and high-energy environment. Results document the CHS and Hosgri Fault in far greater detail and reveal that the CHS is more complex than previously envisioned; however, the additional chronology supports the fault slip rate of 2.6 ± 0.9 mm/yr proposed in Johnson et al. (2014).

THE HOSGRI FAULT AND CROSS-HOSGRI SLOPE

The Hosgri fault is the westernmost active fault within the broader San Andreas Fault System and is the southern portion of the San Gregorio-Hosgri fault system (SGHF, Fig. 1). The SGHF extends along the central California coast for about 360 km and is one of the more active structures within the distributed plate boundary along the west coast of North America (Dickinson et al., 2005). Johnson et al. (2018) recognized three distinct sections of the fault based on different fault azimuths and geomorphology: (1) ~110-km-long southern section, including the CHS, that extends from offshore Point Arguello to San Simeon, has a mean transtensional azimuth of 336° ± 8°, and is characterized by moderate coastal relief, large coastal embayments, the mouths of the Santa Maria and Santa Ynez rivers, and a wider continental shelf, (2) a ~80-km-long middle section (the "Big Sur Bend") that extends from San Simeon to Point Sur, has a mean transpressional azimuth of 321° ± 9°, and is marked by steep coastal relief, small coastal watersheds, and a narrow and deeply incised continental shelf, and (3) a ~170-km-long northern section extends from Point Sur to Bolinas, where the fault converges with the San Andreas fault. The northern section has a mean transtensional azimuth of 337° ± 6° and is generally characterized by lower coastal relief (south of San Andreas fault influence), the large coastal embayment of Monterey Bay, the mouths of the Salinas and Pajaro rivers, and a wider continental shelf.

Based on offset piercing points, SGHF slip rate over the last 10 Ma averages about 14 mm/yr (e.g., Clark, 1997; Dickinson et al., 2005), but this rate must have decreased significantly in the late Neogene. SGHF lateral slip-rate estimates based on late Quaternary features vary and increase from south to north, with a slip rate of about 2.6 mm/yr at the CHS location (Johnson et al., 2014). To the north at San Simeon (Fig. 1), Hall et al. (1994) and Hanson and Lettis (1994) estimated "best constrained" rates of 0.9 to 3.4 mm/yr and 1 to 3 mm/yr , respectively. Johnson

et al. (2018) derived a slip rate estimate of about 3.35 mm/yr based on offset canyons heads offshore Lopez Point in the Big Sur Bend. PG&E (2014) estimated slip rates of 1.6 mm/yr and 1.8 mm/yr in Estero Bay and offshore Point Sal, respectively. These rates are notably lower than the ~11 mm/yr late Quaternary slip rate estimated by Weber (1990) for the SGHF at Point Año Nuevo. Increases in fault slip rate from south to north have been attributed to "adding slip" from northwest-converging faults, including the Lions Head, Casmalia, Shoreline, Oceano, Los Osos, Oceanic, Nacimiento, and Rinconada-Monterey Bay faults (Johnson and Watt, 2012; Langenheim et al., 2013; Watt et al., 2015; Colgan and Stanley, 2016; Johnson et al., 2015; 2018, 2019; Nishenko et al., 2018).

The CHS occurs at ~68 to 76 m water depth in the northern part of the southern SGHF section, about 20 km south of San Simeon and 5 km northwest of Estero Point (Johnson et al., 2014; Figs 1 and 2). In this region the Hosgri fault splits into western and eastern strands, the latter which crosses the CHS (Fig. 2). The CHS has a linear, southwest-facing trend (Fig. 2), a height of 7-9 m, a length of 1700 m, and a width of 250-280 m. The feature is characterized by a slope dipping 1.6° - 2.0° to the SW, a considerably steeper angle than the surrounding seafloor to the northeast and southwest, which dips more gently at 0.4° - 0.6°. Seismic-reflection CHIRP and coring data (see below) indicate the CHS is underlain by post-LGM sediment and is crossed by the main (eastern) strand of the Hosgri fault.

METHODS

High-Resolution CHIRP Data

Approximately 450 km of high-resolution sub-bottom profiles were collected along the central California shelf onboard the M/V *Bold Horizon* in 2019, including 7 profiles across the

CHS (Fig. 2; Snyder et al., 2022). Sub-bottom profiles were collected using an EdgeTech 2300 SB-516 CHIRP system. Initially, deterministic deconvolution processing (match filtering) was conducted onboard the CHIRP to remove the sweep signature from the data. Edgetech output JSF formated files were then converted to SGY to access the raw correlated signal. Processing steps in Shearwater Reveal were applied to the real (non-Hilbert transformed) portion of the data (Henkart, 2006) and included towed depth correction, trace balancing, multi-step static (swell) removal, predictive deconvolution, automatic gain adjustment, and water column mute. As the CHIRP was towed off the starboard side of the ship (vs the stern), predictive deconvolution was applied to remove a short-path multiple likely caused by a reflection off the side of the hull. Horizon mapping and interpretation was done using HIS Kingdom Suite seismic interpretation software.

Bathymetry Data

Bathymetric data used in this study includes high-resolution sonar data collected by the California State University of Monterey Bay Seafloor Mapping Lab (CSUMB) between 2009 and 2010 as part of the California Seafloor Mapping Program (CSUMB, 2012; Johnson et al., 2017). These data consist of a combination of sonar systems that collected data out to 5.6 km offshore (the 3 nautical mile limit California's State Waters). Additional bathymetric data were collected by the USGS in 2012 using a Reson 7111 multibeam sonar that extended coverage beyond the 3 nautical mile limit and included a patch along the CHS (Figure 2; Hartwell et al., 2013).

Sediment Coring and Imaging

A total of 23 sediment cores were collected across the shelf using a Rossfelder P-5 vibracorer, including 6 cores on the CHS, 1 core at about 80 m water depth located below the CHS lower slope break, and 1 core located to the south at 113 m near the shelf break (Fig. 2; Snyder et al., 2022). Cores longer than 1.5 m were split into multiple sections to permit scanning in a Geotek RXCT X-ray tomography system. Full 3D CT scans of all cores were generated, along with XZ and YZ 2D plane slices for each (Fig. 3). Cores were split and then photographed using the Geotek multi-sensor core logger (MSCL) system. P-wave velocity was measured using the MSCL on un-split cores HF-1, HF-3, HF-5, and HF-7, providing a mean velocity of 1617 m/s.

Sand Petrology

Samples from sandy intervals in cores were collected and processed to generate fractions of uniform fine grain size (125-250 microns). Steps included wet sieving, air and oven drying, followed by dry sieving. Standard thin sections with clear epoxy impregnation and potassium feldspar stain were examined petrographically and point counted, 323 to 408 points per sample (Table 1; Snyder et al., 2022).

Radiocarbon Dating

A total of 30 radiocarbon samples and ages were collected from the 7 cores collected in the CHS region (Snyder et al., 2022: Medri et al., 2023). This included 23 gastropod shells, one bivalve shell, and six wood fragments. Gastropods that showed no evidence of reworking were used and species were evaluated to assess habitat (Medri et al., 2023). Radiocarbon ages were determined using atomic mass spectrometry at the University of California Irvin carbon cycle

accelerator mass spectrometer (KCCAMS) facility. ^{14}C ages calculated from shells used the Marine 20 calibration curve of (Heaton et al., 2020) for calibration, whereas wood fragments used the Intcal calibration curve of (Reimer et al., 2020) within the Calib 8.2 program (Stuiver et al., 2022).

Optically Stimulated Luminescence (OSL) Dating

To supplement the radiocarbon dating, we applied OSL dating to determine when quartz grains were last exposed to daylight (Murray et al., 2021). Following the methods of Nelson et al. (2019), we split cores and extracted samples for equivalent dose and dose rate measurements under dark-room conditions. Elemental concentrations were determined by inductively-coupled plasma mass spectrometry on samples immediately above, below, and surrounding the equivalent dose sample and dose rates calculated using the Dose Rate and Age Calculator (Durcan et al., 2015). We applied standard methods to determine the equivalent dose (i.e., Murray et al., 2021) using the single aliquot regeneration protocol (Murray and Wintle, 2000) on <= 2 mm sized masked aliquots of quartz sand. This means that for each aliquot less than 300 grains were analyzed in an averaged luminescence signal (Duller, 2008). OSL characteristics of the samples were favorable with a dominant fast component (Durcan and Duller, 2011) and high percentages of aliquots passed our rejection criteria (Wintle and Murray, 2006). We did not observe substantial evidence of partial bleaching, which would be manifested by high overdispersion and skewed dose distributions (e.g., Fig. 4). We calculated ages using the central age model (CAM) and minimum age model (MAM) from functions in the "luminescence" package for the programming language R (Kreutzer et al., 2013). We found that the CAM produced the best agreement with the radiocarbon ages and thus argue that this model produces

the most accurate, best-bleached exposure age estimates for the sampled core sediment. For additional details and figures related to the methodology please see the supplemental report and Snyder et al. (2022).

RESULTS

Below we present results that establish the stratigraphic and chronologic development of the CHS and characterize fault activity. Within the CHS, Medri et al. (2023) defined three seismic stratigraphic units (S1, S2, S3) above a post-LGM transgressive surface of erosion based on seismic-reflection data, coring, and geochronology. Their S1 unit is here labeled "Unit 1," and their S2 and S3 units are here grouped into our "Unit 2," as described below. The measured mean P-wave velocity of 1,617 m/s is used for time-to-depth conversion for thickness estimates from the CHIRP imaging.

Transgressive Surface of Erosion

Global sea level was about 120 to 130 m lower than present about 21 ka BP during the LGM (Stanford et al., 2011), at which time most of the central California shelf was emergent and the shoreline was at or near the current shelfbreak (Johnson et al., 2019). Landward migration of the shoreline across the ~ 6-km wide emergent shelf in this area is marked by a prominent, shelf-wide, unconformity (Johnson and Watt, 2012; Johnson et al., 2019). This unconformity, a transgressive surface of erosion in seismic-stratigraphic nomenclature (e.g., Catuneanu, 2006), is imaged on CHIRP seismic-reflection profiles as a relatively continuous moderate- to high-amplitude reflection bounding and truncating reflection-free and weakly reflective material below

and an overlying zone of moderate- to high-amplitude discontinuous reflections (Figs. 5, 6, 7, 8). The transgressive surface can be traced across the region from the mid to the outer shelf on CHIRP profiles and was penetrated in four cores collected at water depths of 101 to 113 m. In core HF12, the surface is represented as a shell lag that yielded both pre-LGM and post-LGM radiocarbon dates (e.g., Fig. 8). Such shell lags commonly occur along and above transgressive erosion surfaces as discontinuous scour fills of variable thickness (Catuneanu, 2006), and we infer that they are the source of the high-amplitude reflections common in the lower part of Unit 1 (see below).

Unit 1 Shoreface Deposits

Unit 1 (Unit S1 of Medri et al., 2023) overlies the transgressive surface of erosion, forming the lower stratigraphic unit within the CHS. Unit 1 is characterized by variable seismic facies including parallel to locally divergent, low- to high-amplitude reflections and homogeneous "reflection-free" zones (Figs. 5, 6, 7). Reflections commonly dip offshore about 1.8°, similar to the slope of the CHS seafloor. Laterally, the ~1300-m-long CHIRP profile that extends across the mid-CHS (Fig. 7) shows that the lower boundary of the unit has an erosional, channeled surface, whereas the upper boundary is mostly smooth. The thickness of Unit 1 ranges laterally from about 100 to 310 cm, with much of the variation is due to the channeled relief on the lower erosional boundary. Unit 1's lower and upper boundaries also converge in both the onshore (upslope of the CHS) and offshore (downslope of the CHS) directions, so that the stratigraphic horizon forms a distinct lens with maximum thickness located beneath the CHS (Figs. 5, 6)

Within the CHS, Unit 1 was penetrated the lower 12 cm of HF-1, the lower 24 cm of HF-2, the lower 29 cm of core HF-4, the basal core cutter of HF-3, (Figs. 3, 5A), and in the lower 50 cm in core HF-7, located about 80 m below the CHS lower slope break (Fig. 6B). Medri et al. (2023) describe the cored sediment as the "black sand facies," composed of well-sorted fine-grained sand (mean grain size 130 μm) with less than 5% silt, no clay, and sparse shell fragments. They report that shells within Unit 1 include *Clathurella canfieldi* and *Truncatella californica*, which prefer a sandy habitat, among surf grass roots in the upper intertidal zone (Guz, 2007). Also found was *Turitella Cooperi*, which can occur at intertidal to mid-shelf water depths.

Seismic, sedimentologic, and faunal data indicate Unit 1 was deposited in a shallow water shoreface environment like modern shorefaces along the high-energy California coast (e.g., Barnard et al. 2007, 2009). Seaward-dipping reflections (Figs. 5, 6) indicate primary depositional slope and progradation. Sediment texture (grain size and sorting), the relative lack of infauna, and the significant proportion of heavy minerals (~8.4%, see below) in the sand are also consistent with a high-energy depositional environment.

We obtained nine radiocarbon dates and five OSL dates from unit 1 to constrain its age (Tables 1, 2). Eleven samples are from the upper 28 cm of Unit 1 beneath the CHS in cores HF-1, 2, 3, and 4. Three samples are from the upper 50 cm of unit 1 in core HF-7, located about 80 m below the CHS lower slope break. The mean age of the nine calibrated radiocarbon dates is 10,830 yr B.P with a variation in mean ages ranging from 9,690 to 11,968 yr B.P. The mean age of the five OSL dates is 11.8 ka., with a range of 10.6 ±0.5 to 12.4 ±0.4 ka, and four of the dates fall between 11.8 and 12.4 ka. As discussed above, the OSL dates indicate the time that sand grains were last exposed to sunlight on the beach or in very shallow water, whereas the

radiocarbon dates mainly indicate the time that marine organisms were living on or within the sediment.

Geochronologic data provide a good fit for deposition during or immediately after the Younger Dryas stadial, about 12,800 to 11,500 yr B.P.. The rate of sea-level rise significantly declined during this stadial (Stanford et al., 2011), providing an opportunity for shoreface progradation. All the dates are from the upper 50 cm of a unit that is as thick as 310 cm. Four of the five OSL dates and two of the nine radiocarbon dates fall within the Younger Dryas time interval, five of the seven remaining radiocarbon dates are slightly younger, between ~10,600 and 11,000 yr B.P., and two dates are about 9,700 to 9,800 yr B.P. The younger seven radiocarbon dates are from the uppermost part of the unit and likely reflect late- and post-Younger Dryas physical and biological reworking (e.g., burrowing, grazing) of the upper part of the unit.

Unit 2 – Mid-Shelf Deposits

Unit 2 overlies Unit 1 beneath the CHS (Medri et al., 2023). The lower contact is marked by a discontinuous reflection that coincides with an upward transition from moderate- to high-amplitude reflections at the top of Unit 1 to the zone of diffuse, seafloor-parallel, low- to medium-amplitude reflections that characterize Unit 2 (Figs. 5, 6, 7). The lower contact of Unit 2 is parallel to low-angle discordant, locally truncating reflections in the upper part of Unit 1. The top of Unit 2 is the seafloor.

Unit 2 is up to 300 cm thick, reaching a maximum thickness on the upper CHS (Fig. 5A). Both CHIRP and coring data (Figs. 5, 6) indicate that Unit 2 thins markedly downslope, nearly pinching out at the lower slope break. Paired cores HF-5 and HF-6 on the upper CHS penetrated

a complete 300-cm-thick section of Unit 2. Paired cores HF-3 and HF-4 on the mid slope, and paired cores HF-1 and HF-2 on the lower slope penetrated complete 140-cm- and 80-cm-thick sections, respectively. Core HF-7, located about 80 m below the CHS lower slope break, penetrated a complete 30-cm-thick section of Unit 2. CHIRP profiles (Fig. 5, 6, 7) confirm this downslope thinning, and show variable Unit 2 thinning across the CHS.

Medri et al. (2023) subdivided Unit 2 into 3 distinct subunits based on their sediment characteristics. The lowest subunit consists of 50% sand, 40% silt, and 10% clay, and contains abundant shell fragments throughout. Strata are organized in 10– to 20-cm-thick fining-upward sequences bounded by erosion surfaces. Internally, sediments are parallel- and ripple-laminated. Shell fragments are abundant as are whole shells of gastropods (*Amphissa versicolor, Callianax Baetica*) that commonly occur in mid-shelf water depths (~40 to 70 m). This lower subunit thins from 200 cm in HF-5 on the upper slope, to 70 cm in HF-3 on the mid slope, to 60 cm in HF-1 on the lower slope (Figs 3, 5A). This subunit is not present in core HF-7, located about 80 m below the lower slope break (Figs 2, 6B).

The middle subunit of Unit 2 consists of thin (~2-cm-thick) beds of sandy shell hash comprised of granule to cobble-sized shell fragments in a sandy matrix, bounded by thin beds of parallel-laminated sands. This subunit forms one distinctive, low-angle, ~250-m-wide channel, filled with relatively higher-amplitude reflections, imaged only on the eastern part of the CHS (Figs. 5A, 7A). Where it does occur, the thickness of this subunit decreases from 85 cm in core HF-5 on the upper CHS to 30 cm in HF-3 on the mid CHS, and it is not present in core HF-1 on the lower CHS or in core HF-7, about 80 m below the lower slope break of the CHS. Impedance contrasts associated with the contrasting “hard” shell fragments and “softer” interbeds of fine-

grained sediment are the likely source of the discontinuous, moderate- to high-amplitude reflections that characterize this subunit.

The upper subunit of Unit 2 consists of massive sandy silt with local burrows and scattered shell fragments. This subunit occurs in all the cores, ranging in thickness from 15 cm on the upper CHS in core HF-5, to 40 cm in core HF-3 on the mid CHS, to 20 cm in core HF-1 on the lower slope, to 30 cm in core HF-7 about 80 m below the CHS lower slope break.

We obtained twenty radiocarbon dates and three OSL dates from Unit 2 to constrain its age (Tables 1, 2). The calibrated radiocarbon dates range from about 7,400 yr B.P to Modern, and the OSL dating yields ages of 8.55 to 2.47 ka. We exclude consideration of one out-of-sequence radiocarbon date from HF-5 (~9,400 yr B.P.) because seven deeper samples from this core yielded younger, in-sequence ages, from ~7,400 to 3,400 yr B.P. As noted above, the timing of the onset of Unit 2 deposition (~7,400 yr. B.P.) coincides approximately with the substantial decrease in the rate of sea-level rise, from more than 10 m/1000 years to about 1 m/1,000 years (Peltier and Fairbanks, 2006; Stanford et al., 2011; Reynolds and Simms, 2015). Correlation with global and California sea-level curves indicate unit 2 was deposited at mid-shelf water depths.

Medri et al. (2023) propose that Holocene unit 2 nucleated on the pre-existing relict of a latest Pleistocene (Younger Dryas) shoreface. They infer that sediment transport of the lowest subunit was initiated on the mid shelf by winter-storm waves, with deposition occurring on the CHS as wave-supported gravity flows (WGSF). The overlying shell-hash subunit was interpreted as wave-winnowed shelf deposits. The lowest Unit 2 subunit thins markedly downward on the CHS, and the middle shell-hash subunit pinches out both downward and laterally on the CHS. Medri et al. (2023) interpret the upper Unit 2 sandy silt subunit as a young drape that was deposited by suspension on the CHS and adjacent shelf.

Sand Petrology

Petrographic analysis of fourteen samples of fine-grained sand from Units 1 and 2 is summarized in Table 3 and Figure 9. The siliciclastic framework grain proportions of Unit 1 and Unit 2 are nearly identical (mean QFL = 30,18,52), with somewhat more variation in the upper unit. The sand is derived from the varied bedrock in the Franciscan Complex in the adjacent, southern Santa Lucia Range (Graymer et al., 2014). Prominent Franciscan lithologies in this source area include melange, sandstone, graywacke, conglomerate, greenstone, diabase, chert, serpentinite, and glaucophane schist.

Although the framework of the siliciclastic component of Units 1 and 2 are similar, there are significant differences in the proportions of bioclasts and heavy minerals between the two units. Mean bioclast proportion in Unit 1 and Unit 2 are 5.3% and 31.9%, respectively. Bioclasts consists entirely of shell fragments in Unit 1, but Unit 2 includes both shell fragments and common whole shells (including foraminifera tests). Heavy minerals identified based on color (plain light), relief, pleochroism, and birefringence, include a mix of amphibole (e.g., hornblende) and pyroxene (e.g., augite), and less common mineral types including epidote, sphene, and magnetite. The mean proportion of heavy minerals in Unit 1 and Unit 2 are 8.4% and 2.2%.

The proportions of heavy minerals and bioclasts are consistent with the contrasting depositional environments for Unit 1 and Unit 2. Because of their specific gravity, heavy minerals should have increased presence in a high-energy shoreface environment (Unit 1) that is also not hospitable for significant shell-bearing fauna. In contrast, the inferred mid-shelf environment of Unit 2 provides a less energetic location for shell-bearing fauna (the source of

bioclasts) and is a less likely location for heavy minerals given the need for significant offshore sediment transport.

Hosgri Fault Characterization

The CHIRP profiles that cross the CHS provide ultra high-resolution imagery of the Hosgri fault in the upper 1 to 6 m of the subsurface. Thus, the seismic profiles are representative in scale to roadcut or trench exposures than to seismic-reflection profiles generated by other high-resolution seismic-reflection systems such as mini-sparkers (e.g., Johnson and Watt, 2012; Kluesner et al., 2019). The appearance of the fault varies significantly in the CHIRP imagery within the small CHS area (Fig. 2) as it cuts through different lithologies and stratigraphy at different orientations. Although most motion on the Hosgri Fault is strike slip, the transgressive surface of erosion and the contact between Units 1 and 2 provide markers for documenting apparent vertical fault slip; these markers do not provide information on the more significant strike-slip offset along the fault.

The Hosgri Fault cuts across or is located just below the CHS as exhibited on 3 of the 4 slope-normal CHIRP profiles. Just below the lower slope break on profile HFC-3 (Figs. 2, 5B), the Hosgri Fault is imaged as a sharp contact that warps reflectors in Unit 1, and vertically offsets (up to the west) the transgressive surface of erosion about 110 cm and the shallow (~30 cm deep) Unit 1-Unit 2 contact about 60-70 cm. Based on bathymetric slope profiles, Johnson et al. (2014, their Fig. 10) previously estimated $\geq$ 70 cm (as much as 130 cm) of up-to-the-west vertical offset on the lower slope break along the Hosgri.

Profile HFC-4 images the Hosgri Fault where it crosses the CHS about 20 m below the upper slope break (Figs. 2, 6A). The fault is again imaged as a sharp near-vertical plane,

offsetting the transgressive surface of erosion and the Unit 1-Unit 2 contact about 120 cm and 60 cm, respectively. Profile HFC-2 (Figs. 2, 6B) crosses the Hosgri Fault about 60 m above the CHS upper slope break, imaging the fault as a ~120-m-wide zone of chaotic reflections across which reliable vertical offsets cannot be determined.

Vertical offsets of the Unit 1-Unit 2 contact, along with sediment ages, indicate the Hosgri Fault has been active in the last ~7,000 years. The lack of continuous, traceable internal reflections within Unit 2 limits our ability to discern and measure vertical offsets from any single post-7 ka earthquakes. That the Hosgri Fault does not offset the seafloor on any of the profiles likely indicates that shelf processes (deposition and erosion) have been sufficient to smooth over any vertical relief that might have been generated during the most recent earthquake(s).

DISCUSSION

Depositional Model

The comprehensive geophysical, sedimentologic, and geochronologic data reported above, and the results of Medri et al., 2023, provide the basis for a substantial revision of the Johnson et al. (2014) CHS depositional model. These data suggest the following CHS depositional history, with key stages shown in Figure 10.

A. Rapid sea-level rise from the LGM (~21 ka) to the beginning of the Younger Dryas stadial (~12.8 ka) provided significant accommodation for available coastal sediment supply. A transgressive surface of erosion was generated at the high-energy shoreline, preserved at least locally as a thin shell lag (Fig. 8), the likely source of a nearly continuous, moderate amplitude reflection on CHIRP data (Fig. 4). Clastic sediment derived from the coastal landscape and the

emergent part of the shelf was eroded and redeposited offshore as the shoreline migrated landward.

B. Sea-level rise slowed considerably during the Younger Dryas stadial, which extended from about 12.8 to 11.5 ka (Stanford et al., 2011). As a result, landward migration of the transgressive surface and shoreline slowed and a prograding beach and shoreface developed (Fig. 9B).The CHS lower slope break in Unit 1 occurs at depths of about 73 m below modern sea level and is inferred to represent the base of the shoreface at water depths of about 10 m, based on the depths of modern shorefaces (5 to 15 m) along the California coast (Barnard et al., 2007, 2009). Thus, sea level should have been about 58 to 68 m below present at 11.5 ka when Unit 1 deposition ended. Given the presence of an emergent rocky point at this sea level at the west end of the CHS (Hosgri Ridge on Fig. 2), the prograding beach may have formed a sand spit bounded landward by a lagoon, as suggested by Johnson et al. (2014, their Fig. 7). A preserved portion of this shoreface forms Unit 1 of the CHS, consistent with the sedimentologic, petrologic, and geochronologic data outlined above.

C. Sea level rose rapidly between 11.5 to 7.0 ka (Stanford et al., 2011; Reynolds and Simms, 2015). This change in base level provided abundant accommodation space for deposition of coastal sediment on what is now the inner continental shelf, effectively shutting down sediment supply to the progressively deeper CHS. The upper part of the Younger Dryas beach-shoreface complex was eroded and reworked by wave energy in the earliest part of this time-period, forming the erosional surface on seismic reflection profiles that represents the contact between Units 1 and 2 (Figs. 5, 6, 7). The sediment-starved, wave-erosion surface and underlying uppermost part of Unit 1 were then colonized by shallow-water fauna, providing the material that yielded radiocarbon dates slightly younger than the Younger Dryas depositional age

of unit 1 (Table 1). The wave-erosion surface converges with the underlying transgressive surface of erosion both seaward and landward of the CHS, so that the Unit 1 shoreface was buried by younger sediment and preserved as an elongate lens.

D. From about 7.0 ka to the present, the rate of sea-level rise dramatically decreased to about 1 m/1,000 years (Reynolds and Simms, 2015). The effects of this decrease included: (1) a substantial decrease in the rate of creation of new sediment accommodation space, and (2) an associated increase in the time available for offshore shelf-sediment transport. The net result was movement of coastal sediment to mid-shelf environments and deposition of Unit 2 mid-shelf deposits as a low-angle clinoform above the relict CHS shoreface (Medri et al., 2023).

Hosgri Fault Slip Rate and Earthquake History

Determining the slip-rate of a strike-slip fault requires documentation of the amount of lateral slip of a piercing point, and the time-period over which that slip occurred. Johnson et al. (2014) showed that the lower slope break of the CHS was a mappable, linear geomorphic feature that crossed the Hosgri Fault, forming a unique piercing point (Fig. 2 inset). Understanding the development and history of the CHS lower slope break (Fig. 10) is thus essential for developing and (or) revising a Hosgri Fault slip rate.

Previously, Johnson et al. (2014) inferred that the CHS was underlain by a relict Younger Dryas (latest Pleistocene) shoreface deposit (i.e., Unit 1 of this study), and noted lateral offset of both the lower and upper slope breaks. The offset was determined by plotting data points and regression lines obtained from normal-to-slope profiles located 12.5 m apart (Fig. 2; Johnson et al., 2014, their Figs. 8, 9, 10, 11). They restricted the slip-rate analysis to a set of 34 (of 93)

455 points located on slope profiles from 225 m west of the fault trace to 200 m to the east of the
456 fault, to limit the influence of slope curvature and (or) the depositional or erosional irregularities
457 that occur along the lower slope break farther from the fault. They considered the lower slope
458 break (the inferred base of the paleoshoreface) as a far more reliable piercing point because, as
459 sea level rose in the latest Pleistocene, it would sink earlier below wave base and thereby would
460 have experienced less reworking by storm waves and subsequent sedimentation. They measured
461 30.3 ± 9.4 m of lateral offset of the lower slope break based on the slope profiles, an amount
462 similar to their estimate (34 m) based on a simpler analysis of digital elevation models and slope
463 maps derived from high-resolution bathymetric surveys (Johnson et al., 2014, their Fig. 8).
464 The new data presented in this study show that the Johnson et al. (2014) analysis
465 significantly underestimated the amount of erosion of the latest Pleistocene Unit 1 shoreface
466 deposits and were not aware of the thickness and sedimentology of the overlying Unit 2 middle
467 to late Holocene mid-shelf deposits (Medri et al., 2023). This new information is incorporated in
468 the depositional model of Figure 10, providing essential context for understanding the origin and
469 history of the lower slope break and its viability as a piercing point.
470 Together, the CHIRP (Figs. 5,6,7) and core data (Fig. 3) indicate that the lower slope
471 break represents the base of the Unit 1 shoreface (Fig. 10B, C), covered by downslope-thinning
472 Unit 2 shelf deposits (Fig. 10D). In the 425-m-wide local area Johnson et al. (2014) used to
473 measure fault offset, Unit 2 thickness decreases from about 108 to 124 cm thick along the HF-
474 25b profile (Fig. 2), to about 81 to 88 cm in cores HF-1 and HF-2 about 20 m farther downslope
475 (Figs. 2, 3). Unit 2 is about 50 to 60 cm thick at the lower slope break, and finally to about 30
476 cm, 80 m seaward of the CHS lower slope break in core HF-7 (Medri et al. 2023). Core and
477 CHIRP data indicate that at the lower slope break, the 50-60 cm of Unit 2 consists of about half

lower subunit (wave supported gravity flow deposits) and about half suspension deposits of the upper subunit. In addition, no significant change in Unit 2 thickness is observed across the fault zone on CHIRP profile HFC-25b (Fig. 7B), which is the closest and approximately parallel profile to the lower slope break points used by Johnson et al., 2014 (Fig. 2).

Given the density of CHIRP profile lines and the number and location of cores collected, we cannot quantify the amount (if any; see Fig. 7B) of variation in Unit 2 thickness across the local CHS area that was used to determine lateral fault slip (Fig. 2). For our slip-rate analysis, we therefore assume the Unit 2 thicknesses outlined above is uniform in this local, fault-adjacent area. Thus, simple uniform removal of the thin Unit 2 cover does not change the locations of the lower slope break relative to one another on bathymetric slope profiles, so the amount of estimated lateral offset of this linear feature determined by Johnson et al. (2014) remains valid. The thin Unit 2 drape (Fig. 10D) may slightly smooth the lower slope break (Fig. 10D), but it does not compromise its value as a piercing point.

Given issues with small (~1°) slope changes, projections, and rounding errors, Johnson et al. (2014) estimated that uncertainties in locating the lower slope break based on slope profiles could be as much as 10 m for some data points, but that the effects of such errors were minimized by analyzing large numbers of slope profiles at tight profile spacing. For our assessment, it seems possible that undetected variations in Unit 2 thickness could lead to greater uncertainty in locating the minimally buried base of the latest Pleistocene shoreface, but that increase cannot be quantified with the current data.

The OSL and radiocarbon dates reported herein strongly support a Younger Dryas age, ~12,800 to 11,500 yr. B.P., for the latest Pleistocene shoreface (Unit 1 above), with the end of

shoreface deposition resulting from rapid sea-level rise at the onset of Meltwater Pulse 1B (e.g., Alley, 2000; Stanford et al., 2013; Liu and Milliman, 2004). There are variable estimates of sea-level rise following the Younger Dryas. Stanford and others (2011) described Meltwater Pulse 1B as "robustly expressed," a multi-millennial interval of enhanced rates between 11,500 and 8,800 calendar years ago with peak rates of rise of up to 25 m/1,000 yrs. Using 11,500 yr B.P. as the age of the CHS lower slope break and 30.3 ± 9.4 (two standard deviations, 95% confidence limit) as the amount of offset yields a slip rate of 2.6 ± 0.8 mm/yr, essentially the same as the previously suggested rate of 2.6±0.9 mm/yr (Johnson et al., 2014). The previous rate was determined using a Monte Carlo simulation in which the age of the lower slope break was assigned a range of 12,000 ± 500 years, so that possible slip ranged from 20.9 m in 12,500 years to 39.7 m in 11,500 years. The wealth of new geochronologic data obtained for this study (Tables 2, 3) reduces age uncertainty and makes the simpler and more direct statistical methodology approach we use in this study feasible.

CHIRP profiles clearly indicate Holocene (since at least ~7 ka) activity of the Hosgri fault. Reflection-defined surfaces interpreted as the latest Pleistocene transgressive surface of erosion and an early Holocene wave-erosion surface (Unit 1-Unit 2 contact) are vertically offset on all fault crossings (Figs. 5, 6, 7). The amount of vertical offset is consistently larger for the older surfaces, although the amounts of vertical offset on each surface varies from profile to profile. Maximum offsets for the transgressive surface and wave-erosion surface are 125 cm and 73 cm.

Advances in Geophysical Imaging and Geochronology

Conducting paleoseismology in the marine environment is difficult, with a significant portion of studies relying on secondary evidence of fault activity (e.g., turbidites; Goldfinger, 2011) or the correlation of offset sedimentary features to approximated sea-level curves to provide timing constraints (e.g., Johnson et al., 2014, Nishenko et al., 2018). However, ultra-high-resolution sub-bottom geophysical imaging, combined with precise age control from dated sediment cores, offers the opportunity to provide primary, near-field evidence of time-constrained coseismic fault offset (e.g., Brothers et al., 2011;2015, Watt et al., 2016).

Although Johnson et al. (2014) used single-channel sparker data to image and interpret the CHS, CHIRP results from this study show that the sparker data lacks the vertical resolution needed to make accurate interpretations of the post-LGM stratigraphy (Fig. 11A). Furthermore, most offshore CHIRP studies utilize "envelope" imagery output by acquisition systems for the final interpreted image. Such envelope imagery is composed of the original or "real" signal merged with an "imaginary" signal, a 90° phase-shifted version (Hilbert transform) of the real signal (Henkart, 2006). This envelope combination results in only positive amplitudes, loss of polarity information, and a lower frequency/resolution image than is possible with more advanced processing (Baradello, 2014). In this study we observed that when processing the "real" or full-waveform CHIRP data, extra care must be taken in calculating static (swell) corrections and deconvolution, so that the high-frequency polarity-preserved reflections align properly from trace to trace. Doing so preserves the lateral high-resolution content and layering, which can be easily lost with less optimal processing. This is especially important for mapping seismic stratigraphy and fault offsets in coarse-grained, marginally stratified, or extensively bioturbated sediments, where signal penetration can be limited, and strata commonly show minimal impedance contrasts. The shoreface and mid-shelf deposits of our study provide good

examples of difficult to image depositional systems where advanced processing can be especially important.

When comparing the envelope to the full-waveform processed CHIRP data along profile HFC-4, the difference in geological resolvability is stark (Fig. 11b, 11c). For example, on the envelope processed version of HFC-4 the offset of the shoreface deposit (Unit 1) by the Hosgri fault is nearly impossible to resolve (Fig. 11b), whereas this can be confidently interpreted, and offsets measured on the full waveform data (Fig. 11c). Similarly, clearly resolving the transgressive surface of erosion and internal progradational bedding of the shoreface deposit (Unit 1) is difficult at best on the envelope-processed data (Fig. 11b). No evidence of offset, nor internal shoreface deposit patterns are discernable on the sparker profile, which is also marred by short period multiples (Fig. 11a) that are characteristic of this source (Kluesner et al., 2019). These comparative subbottom profiles show that when attempting to image and study recent or active faulting of Holocene sediments, special care must be taken in selecting the proper sound source, as well as processing the data to the fullest potential.

Although it is common practice for terrestrial paleoseismic work to use the combination of radiocarbon and OSL dating techniques (e.g., Gray et al., 2015; Bennett et al., 2018; DuRoss et al., 2022), this approach is currently in the incipient stages for offshore paleoseismic studies, with this study being the first known application. Other offshore sedimentological studies have looked at sediment ages with both radiocarbon and OSL techniques (e.g., Alappat et al., 2010; Yi et al., 2013; Yang et al., 2015), including a study of sediment transport down the Monterey canyon system, offshore central California (Stevens et al., 2013). Stevens et al., 2013 found that differences in OSL and radiocarbon ages indicated sediment transport timing varied from decadal (canyon head)- to millennial (>1.1 km depth)-scale transport down the canyon system.

In contrast, our study involves a somewhat different environment that includes on a relict shoreface deposit and issues of mid-shelf sediment transport. We find generally good agreement between radiocarbon and OSL CAM model ages, with OSL generally producing slightly older ages. For example, within Unit 1 the mean OSL age is ~ 1,000 yr older than the mean radiocarbon age. As discussed earlier, this time gap may reflect the time between last quartz grain sun exposure on land or shallow water and when the dated radiocarbon material was deposited in deeper water. Another possibility is that the OSL was incompletely reset prior to deposition with an inherited 1000 years of apparent age, although we did not see strong evidence for partial bleaching. It is also worth noting that we assumed full saturated water content over the OSL burial period. It is possible that the sampled sediment was drier during the subaqueous episode prior to eustatic sea level rise. This unknown drier period would result in a slightly high dose rate for that period and a slight overestimation of the true burial age. However, the generally good correspondence between radiocarbon and OSL suggests that the assumptions behind OSL dating are applicable in this environment. This study shows that combining the two techniques can provide additional information to help resolve the depositional history and further strengthen the geochronological model, both of which are crucial when conducting offshore paleoseismic studies.

CONCLUSIONS

New data obtained from CHIRP seismic reflection profiles and shallow sediment cores provide the basis for a reassessment of the slip rate of the Hosgri Fault offshore central California. The Hosgri fault cuts the cross-Hosgri slope (CHS), a subtle seafloor lineament

previously interpreted as a latest Pleistocene (Younger Dryas, ~12.8 to 11.5 ka) shoreface deposit. Offset of the lower slope break of this inferred shoreface provided the basis for inferring a lateral slip rate of 2.6 ± 0.9 mm/yr. The CHS has a complex depositional history that comprises two distinct stratigraphic units. The lower unit (Unit 1) overlies the post-LGM transgressive surface of erosion and is interpreted as a shoreface deposit based on seismic facies (offshore-dipping reflections), sediment texture (clean fine sand), sediment infauna, and significant component (~8.4%) of heavy minerals. Radiocarbon and OSL dates from the top of Unit 1 are consistent with deposition during the Younger Dryas. The shoreface was abandoned and partly eroded during the subsequent pulse of rapid sea-level rise and transgression that ended about 7 ka. Unit 2 consists of fine to very fine sand and silt deposited in a mid-shelf environment between ~ 7 ka and the present, when the rate of sea-level rise slowed dramatically. Deposition primarily occurred as wave-supported gravity flows transported sandy sediment down the pre-existing shoreface slope, and through deposition of muddy sediment from suspension (Medri et al., 2023). Although Unit 2 provides a thin (~50 - 60 cm) cover over the lower slope break of the shoreface, it does not compromise the value of this feature as a piercing point and the previously proposed slip rate remains valid. This work benefitted significantly from full-waveform processing of CHIRP data, resulting in significantly higher resolution in coarser grained strata that are typically difficult to image; application of these techniques should have importance in neotectonic studies of shelf and high-energy environments elsewhere. Our novel combination of radiocarbon and OSL dating also provided important insights into depositional history and strengthened the geochronological model, both of which can have similar value in other offshore paleosiesmic investigations.

ACKNOWLEDGMENTS

Support for this work was provided by the USGS Coastal and Marine and Resources Program and by Pacific Gas and Electric through a Cooperative Research and Development Agreement. We would like to thank Alicia Balster-Gee, George Snyder, Rachel Marcuson, Daniel Powers, Jennifer McKee, Cordell Johnson, and the crew of the M/V *Bold Horizon*. This material is also based upon work supported by the U.S. Geological Survey under Grant No. G20AS00042 to ARS. Any use of trade, product, or firm names is for descriptive purposes only and does not imply endorsement by the U.S. Government.

REFERENCES CITED

Alappat, L., Vink, A., Tsukamoto, S., and Frechen, M., 2010, Establishing the Late Pleistocene–Holocene sedimentation boundary in the southern North Sea using OSL dating of shallow continental shelf sediments. Proceedings of the Geologists' Association, v. 121, p. 43–54, https://doi.org/10.1016/j.pgeola.2009.12.006.

Alley, R.B., 2000, The Younger Dryas cold interval as viewed from central Greenland, Quaternary Science Review, v. 19, p. 213-226, https://doi.org/10.1016/S0277-3791(99)00062-1.

Barnard, P.L., Eshleman, J., Erikson, L., and Hanes, D.M., 2007, Coastal processes study at Ocean Beach, San Francisco, CA: Summary of data collection 2004–2006, U. S. Geol.

Surv. Open-File Rept. 2007-1217, 171 p., http://pubs.usgs.gov/of/2007/1217/ (last accessed October 2022).

Barnard, P.L., Revell, D.L., Hoover, D., Warrick, J., Brocatus, J., Draut, A.E., Dartnell, P., Elias, E., Mustain, N., Hart, P.E., and Ryan, H.F., 2009, Coastal processes study of Santa Barbara and Ventura Counties, California, U.S. Geol. Surv. Open-File Rept. 2009-1029, 926 p., http://pubs.usgs.gov/of/2009/1029/ (last accessed October 2022).

Baradello, L., 2014, An improved processing sequence for uncorrelated Chirp sonar data, Marine Geophysical Research, v. 35, p. 337-344, https://doi.org/10.1007/s11001-014-9220-1

Bennett, S.E.K., DuRoss, C. B., Gold, R. D., Briggs, R. W., Personius, S. F., Reitman, N. G., et al. (2018). Paleoseismic results from the Alpine site, Wasatch fault zone: Timing and displacement data for six Holocene earthquakes at the Salt Lake City-Provo segment boundary. Bulletin of Seismological Society of America, v. 108, p. 3202–3224, https://doi.org/10.1785/0120160358.

Brothers, D.S., Kilb, D., Luttrell, K., Driscoll, N.W., and Kent, G.M., 2011, Loading of the San Andreas fault by flood-induced rupture of faults beneath the Salton Sea, Nature Geoscience, v. 4, p. 486–492, https://doi.org/10.1038/ngeo1184.

Brothers, D.S., Conrad, J.E., Maier, K.L., Paull, C.K., McGann, M, and Caress, D.W., 2015, The Palos Verdes Fault offshore Southern California: Late Pleistocene to present tectonic

geomorphology, seascape evolution, and slip rate estimate based on AUV and ROV surveys, Journal of Geophysical Research: Solid Earth, v. 120, p. 4734–4758, https://doi.org/10.1002/2015JB011938.

California State University Monterey Bay Sea Floor Mapping Lab (CSUMB), 2012, Seafloor Mapping Lab at CSUMB, https://csumb.edu/undersea/seafloor-maps/ (last accessed November 2022).

Catuneanu, O., 2006, Principles of Sequence Stratigraphy, Elsevier, Amsterdam, The Netherlands, 375 pp.

Clark, J.C., 1997, Neotectonics of the San Gregorio Fault Zone—Age dating controls on offset history and slip rate (Final Tech. Rep., National Earthquake Hazards Reduction Program, Award No. 1434-HQ-96-GR-02741), 19 pp.

Colgan, J.P., and Stanley, R.G., 2016, The Point Sal–Point Piedras Blancas correlation and the problem of slip on the San Gregorio–Hosgri fault, central California Coast Ranges, Geosphere, v. 12, p. 971–984. https://doi.org/10.1130/GES01289.1.

Dickinson, W.R., Ducea, M.N., Rosenberg, L.I., Greene, H.G., Graham, S.A., Clark, J.C., Weber, G.E., Kidder, S., Ernst, W.G., and Brabb, E.E., 2005, Net dextral slip, Neogene San Gregorio–Hosgri fault zone, coastal California: Geologic evidence and tectonic

implications. Geological Society of America Special Paper 391, https://doi.org/10.1130/SPE391.

Duller, G.A., 2008, Single-grain optical dating of Quaternary sediments: why aliquot size matters in luminescence dating, Boreas, v. 37, p. 589-612.

Durcan, J.A., King, G.E., and Duller, G.A., 2015, DRAC: Dose Rate and Age Calculator for trapped charge dating, Quaternary Geochronology, v. 28, p. 54-61, https://doi.org/10.1016/j.quageo.2015.03.012.

Durcan, J.A., and Duller, G.A., 2011, The fast ratio: A rapid measure for testing the dominance of the fast component in the initial OSL signal from quartz, Radiation Measurements. v. 46, p. 1065-1072, https:// 10.1016/j.radmeas.2011.07.016.

DuRoss, C.B., Gold, R.D., Gray, H.J., and Nicovich, S.R., 2022, Portable optically stimulated luminescence age map of a paleoseismic exposure, Geology, v. 50, p. 470–475, https://doi.org/10.1130/G49472.1.

Galbraith, R.F., and Roberts, R.G., 2012, Statistical aspects of equivalent dose and error calculation and display in OSL dating: An overview and some recommendations, Quaternary Geochronology, v. 11, p. 1-27, https://doi.org/10.1016/j.quageo.2012.04.020.

Goldfinger, C. (2011). Submarine paleoseismology based on turbidite records, Annual Review of Marine Science, v. 3, 35–66, https://doi.org/10.1146/annurev-marine-120709-142852.

Gray, H.J., Mahan, S.A., Rittenour, T.M., and Nelson, M.S., 2015, Guide to luminescence dating techniques and their application for paleoseismic research, in Lund, W.R., ed., Proceedings, Basin and Range Province Seismic Hazards Summit III: Utah Geological Survey and Western States Seismic Policy Council, 18 p.

Graymer, R. W., V.E. Langenheim, M. A. Roberts, and K. McDougall (2014). Geologic and geophysical maps of the eastern three-fourths of the Cambria $30^0 \times 60^0$ quadrangle, central California Coast Ranges, scale 1:100,000, U.S. Geological Survey Scientific Investigation Map 3287, 50 p. https://doi.org/10.3133/sim3287.

Guz, S.S., 2007, The light and smith manual: Intertidal invertebrates from Central California to Oregon. Libr. J. 132, 154 p.

Hall, N.T., Hunt, T.D., and Vaughan, P.R., 1994, Holocene behavior of the San Simeon fault zone, south-central coastal California, in Seismotectonics of the Central California Coast Ranges, I.B. Alterman, R.B. McMullen, L.S. Cluff, and D.B. Slemmons (Editors), Geological Society of America Special Paper 292, Boulder, Colorado, p. 167–189.

Hanson, K.L., and Lettis, W.R., 1994, Estimated Pleistocene slip rate for the San Simeon fault zone, south-central coastal California, in Seismotectonics of the Central California Coast Ranges, I.B. Alterman, R.B. McMullen, L.S. Cluff, and D B. Slemmons (Editors), Geological Society of America Special Paper 292, Boulder, Colorado, p. 133–150.

Hanson, K.L., W.R. Lettis, M.K. McLaren, W.U. Savage, and N.T. Hall (2004). Style and rate of Quaternary deformation of the Hosgri fault zone, offshore south-central California, U.S. Geoloical Survey Bulletin 1995BB, 33 pp., https://doi.org/10.3133/b1995BB.

Hartwell, S.R., Finlayson, D.P., Dartnell, P., and Johnson, S.Y., 2013, Bathymetry and acoustic backscatter, Estero Bay, California, U.S. Geological Survey Open-File Report 2013-1225, http://pubs.usgs.gov/of/ 2013/1225/abstract.html (last accessed November 2022).

Heaton, T. J., Köhler, P., Butzin, M., Bard, E., Reimer, R.W., Austin, W.E.N., Ramsey, C.B., Grootes, P.M., Hughen, K.A., Kromer, B., Reimer, P.J., Adkins, J., Burke, A., Cook, M.S., Olsen, J., and Skinner, L.C., 2020, Marine20—The Marine Radiocarbon Age Calibration Curve (0–55,000 cal BP). Radiocarbon**,** v. 62, p. 779-820. https://doi.org/10.1017/RDC.2020.68.

Henkart P., 2006, Chirp sub-bottom profiler processing—a review, Sea Technology, v. 47, p. 35–38.

Johnson, S.Y., and Watt, J.T., 2012, Influence of fault trend, bends, and convergence on shallow structure and geomorphology of the Hosgri strike-slip fault, offshore central California, Geosphere, v. 8, p. 1632-1656, https://doi.org/10.1130/GES00830.1.

Johnson, S.Y., Hartwell, S.R., and Dartnell, P., 2014, Offset of Latest Pleistocene Shoreface Reveals Slip Rate on the Hosgri Strike-Slip Fault, Offshore Central California. Bulletin of Seismological Society of America, v. 104, p. 1650-1662. https://doi.org/10.1785/0120130257.

Johnson, S.Y., Hartwell, S.R., and Davenport, C.W., 2015, Offshore and onshore geology and geomorphology, Offshore of Santa Cruz map area, California, sheet 10, scale 1:24,000. In G. R. Cochrane and S. A. Cochran (Editors.), California State Waters Map Series—Offshore of Santa Cruz, California, U.S. Geological Survey Open-File Report 2015–1024, 40 p, 10 sheets. https://doi.org/10.3133/ofr20151024.

Johnson, S.Y., Cochran, G.R., Golden, N.E., Dartnell, P., Hartwell, S.R., Cochran, S.A., Watt, J.T., 2017, The California Seafloor and Coastal Mapping Program – Providing science and geospatial data for California's State Waters, Ocean & Coastal Management, v. 140, p. 88–104, https://doi.org/10.1016/j.ocecoaman.2017.02.004 .

Johnson, S.Y., Watt, J.T., Hartwell, S.R., and Kluesner, J.W., 2018, Neotectonics of the Big Sur Bend, San Gregorio-Hosgri Fault System, Central California, Tectonics, v. 37, p. 1930-1954, https://doi.org/10.1029/2017TC004724.

Johnson, S.Y., Hartwell, S.R., Watt, J.T., Beeson, J.W., and Dartnell, P., 2019, Offshore shallow structure and sediment distribution, Point Sur to Point Arguello, central California, U.S. Geological Surveuy Open-File Report 2018–1158, 3 sheets, scales 1:150,000 and 1:200,000. https://doi.org/https://doi.org/10.3133/ofr20181158.

Kluesner, J., Brothers, D., Hart, P., Miller, N., and Hatcher, G., 2019, Practical approaches to maximizing the resolution of sparker seismic reflection data, Marine Geophysical Research, v. 40, p. 279-301, https://doi.org/10.1007/s11001-018-9367-2.

Kreutzer, S., Schmidt, C., Fuchs, M.C., Dietze, M., Fischer, M., and Fuchs, M., 2012, Introducing an R package for luminescence dating analysis, Ancient TL, v. 30, p. 1-8.

Liu, J.P., and Milliman, J.D., 2004, Reconsidering melt-water pulses 1A and 1B: global impacts of rapid sea-level rise, Journal of Ocean University of China, v. 3, p. 183-190.

Langenheim, V.E., Jachens, R.C., Graymer, R.W., Colgan, J.P., Wentworth, C.M., and Stanley, R.G., 2013, Fault geometry and cumulative offsets in the central Coast Ranges, California: Evidence for northward increasing slip along the San Gregorio-San Simeon-Hosgri fault. Lithosphere, v. 5, p. 29-48, https://doi.org/10.1130/L233.1

Medri, E., Simms, A.R., Kluesner, J., Johnson, S.Y., Nishenko, S.P., Greene, H.G., and Conrad, J.E., 2022, Subaqueous clinoforms created by sandy wave-supported gravity flows:

lessons from the central California shelf, Marine Geology, v. 456, 13 p., https://doi.org/10.1016/j.margeo.2022.106977.

Murray, A.S., and Wintle, A.G., 2000, Luminescence dating of quartz using an improved single-aliquot regenerative-dose protocol, Radiation Measure, v. 32, p. 57-73.

Murray, A., Arnold, L.J., Buylaert, J.P., Guérin, G., Qin, J., Singhvi, A.K., Smedley, R., and Thomsen, K.J., 2021, Optically stimulated luminescence dating using quartz. Nature Reviews Methods Primer, v. 1, p. 1-31.

Nelson, M., Rittenour, T., and Cornachione, H., 2019, Sampling methods for luminescence dating of subsurface deposits from cores. Methods and Protocols, v. 2, 88, https://doi.org/10.3390/mps2040088.

Nishenko, S., Greene, H.G., Hogan, P., and Bergkamp, B., 2018, Geometry and Late Pleistocene Displacement of the Shoreline and Oceano Fault Zones, San Luis Obispo Bay, California, Bulletin of the Seismological Society of America, v. 108**,** p. 3225-3247, https://doi.org/10.1785/0120160177.

Pacific Gas and Electric Company (PG&E), 2014, Offshore low-energy seismic reflection studies in Estero Bay, San Luis Obispo Bay, and Point Sal Areas: PG&E Technical Report, GEO.DCPP.TR.14.02, available at

http://www.pge.com/includes/docs/pdfs/safety/systemworks/dcpp/report/Ch3.GEO.DCPP.TR.14.02_R0_txt.w.ITR.pdf https://www.pge.com/includes/docs/pdfs/safety/systemworks/dcpp/report/Ch3.GEO.DCPP.TR.14.02_R0_Figures.pdf.

Peltier, W.R., and Fairbanks, R.G., 2006, Global glacial ice volume and last glacial maximum duration from an extended Barbados sea level record, Quaternary Science Reviews, v. 25, p. 3322–3337, https://doi.org/10.1016/j.quascirev.2006.04.010.

Reimer, P.J., Austin, W.E.N., Bard, E., Bayliss, A., Blackwell, P.G., Ramsey, C.B., Butzin, M., Cheng, H., Edwards, R.L., Friedrich, M., Grootes, P.M., Guilderson, T.P., Hajdas, I., Heaton, T.J., Hogg, A.G., Hughen, K.A., Kromer, B., Manning, S.W., Muscheler, R., and Talamo, S., 2020, The IntCal20 Northern Hemisphere Radiocarbon Age Calibration Curve (0–55 cal kBP). Radiocarbon, v. 62, p. 725-757, https://doi.org/10.1017/RDC.2020.41.

Reynolds, L.C., and Simms, A.R., 2015, Late Quaternary relative sea level in southern California and Monterey Bay, Quaternary Science Reviews, v. 126, p. 57-66, https://doi.org/10.1016/j.quascirev.2015.08.003.

Stanford, J.D., Hemingway, R., Rohling, E.J., Challenor, P.G., Medina-Elizalde, M., and Lester, A.J., 2011, Sea-level probability for the last deglaciation: A statistical analysis of far-field records, Global Planetary Change, v. 79, p. 193–203, https://doi.org/10.1016/j.gloplacha.2010.11.002.

Stevens, T., Paull, C.K., Ussler, W., McGann, M., Buylaert, J.P., and Lundsten, E., 2013, The timing of sediment transport down Monterey Submarine Canyon, offshore California. GSA Bulletin, v. 126, (1-2), p. 103–121, https://doi.org/10.1130/B30931.1.

Stuiver, M., Reimer, P.J., and Reimer, R.W., 2022, CALIB 14C Calibration Program. [WWW program] at http://calib.org

Snyder, G.R., Balster-Gee, A.F., Kluesner, J.W., Johnson, S.Y., Medri, E., Simms R.A., Nishenko, S., Greene, G., and Conrad, J.E., 2022, Geophysical and core sample data collected offshore central California, during field activity 2019-651-FA, U.S. Geological Survey Data Release, https://doi.org/https://doi.org/10.5066/P9A0U8J7

Walton, M.A.L., Papesh, A.G., Johnson, S.Y., Conrad, J.E., and Brothers, D.S., 2020, Quaternary faults offshore of California, U.S. Geological Survey Data Release, https://doi.org/10.5066/P91RYEZ4.

Watt, J.T., Johnson, S.Y., Hartwell, S.R., and Roberts, M., 2015, Offshore geology and geomorphology maps from Piedras Blancas to Pismo Beach, California. U.S. Geological Survey Scientific Investigations Map 3327, 6 sheets, scale 1:35,000, http://pubs.usgs.gov/sim/3327/

Watt, J.T., Ponce, D., Parsons, T., and Hart, P., 2016, Missing link between the Hayward and Rodgers Creek Faults, Science Advances, v. 2, e160144, https://doi.org/10.1126/sciadv.1601441.

Weber, G.E., 1990, Late Pleistocene slip rates on the San Gregorio Fault Zone at Point Año Nuevo, San Mateo County, California. In R. E. Garrison, et al. (Eds.), Geology and tectonics of the central California Coast Region, San Francisco to Monterey, Volume and Guidebook, R.E. Garrison, H.G. Greene, K R. Hicks, G E. Weber, and T.L. Wright (Editors), Pacific Section of the American Association of Petroleum Geologists, Bakersfield, California, p. 193–204.

Wintle, A.G., and Murray, A.S., 2006, A review of quartz optically stimulated luminescence characteristics and their relevance in single-aliquot regeneration dating protocols. Radiation Measurements, v. 41, p. 369-391, https://doi.org/10.1016/j.radmeas.2005.11.001.

Yang, L.H., Long, H., Yi, L., Li, P., Wang, Y., Gao, L., and Shen, J., 2015, Luminescence dating of marine sediments from the Sea of Japan using quartz OSL and polymineral pIRIR signals of fine grains, Quaternary Geochronology, v. 30, p. 257–263, https://doi.org/10.1016/j.quageo.2015.05.003

Yi, L., Lai, Z., Yu, H., Xu, X., Su, Q., Yao, J., Wang, X., and Shi, X., 2013, Chronologies of Sedimentary Changes in the South Bohai Sea, China, Constraints from Luminescence and Radiocarbon Dating, v. 42, p. 267–284. https://doi.org/10.1111/j.1502-3885.2012.00271.x.

887 TABLES

888

UCIAMS #	Core	Depth (cm)	Material/species	D^{14}C ‰	±	^{14}C age	±	Calibrated age (Cal years B.P.)
254929	HF-1	46	*Amphissa versicolor*	-186.7	1.3	1660	15	1180-917
254931	HF-1	61	*Neverita lewiisi*	-519.68	1.0	5890	20	**6264-5961***
254930	HF-1	80	*Amphissa versicolor*	-408.7	1.3	4220	20	4295-3955
254932	HF-1	90	*Clathurella canfieldi*	-705.8	0.6	9825	20	10774-10442
254936	HF-1	97	*Truncatella californica*	-734.9	0.6	10665	20	12027-11623
260440	HF-2	103.5	Gastropod	-730.1	0.7	10520	25	11808-11386
260441	HF-2	106	Gastropod	-712.3	0.7	10010	20	11085-10714
246214	HF-3	Cutter nose	*Callianax baetica*	-710.30	0.7	9950	20	11044-10640
230405	HF-3	VC cutter nose	*Gastropod*	-714.6	0.9	10075	25	11163-10795
243289	HF-3	137	*Amphissa versicolor*	-555.3	0.8	6510	15	6940-6634
230406	HF-3	131	*Gastropod*	-568.3	1.1	6750	25	7224-6901
243298	HF-3	110	Wood	-213.6	1.2	1930	15	1924-1794
243290	HF-3	80	Bivalve	-196.2	1.4	1755	15	1279-1025
243291	HF-3	40	*Amphissa versicolor*	-140.9	1.5	1220	15	721-515
260442	HF-4	154	*Turritella cooperi*	-683.2	0.7	9235	20	10035-9620
260443	HF-4	171.5	Gastropod	-679.2	0.7	9135	20	9857-9524
243299	HF-5	115	Wood	-265.7	1.2	2480	15	**2710-2473***
243292	HF-5	122	*Amphissa versicolor*	-183.2	1.3	1625	15	1157-898
254938	HF-5	155	*Amphissa versicolor*	-267.4	1.2	2500	15	2125-1835
254933	HF-5	166	*Amphissa versicolor*	-243.7	1.2	2245	15	1808-1534
254935	HF-5	175	*Callianax baetica*	-670.7	0.6	8920	20	**9532-9301***
254945	HF-5	180	Wood	-323.6	1.1	3140	15	3441-3272
254944	HF-5	199	Wood	-309.4	1.1	2975	15	3211-3076
254937	HF-5	222	*Amphissa versicolor*	-434.4	0.9	4575	15	4776-4434
246230	HF-5	233	Wood	-451.8	0.9	4830	15	5594-5484
243293	HF-5	255	*Callianax baetica*	-561.5	0.7	6625	15	7088-6749
243300	HF-5	287	Wood	-492.6	0.9	5450	15	**6295-6207***
260444	HF-5	296	*Turritella cooperi*	-586.1	0.9	7085	20	**7516-7257**
254934	HF-7	20	*Amphissa versicolor*	8.2	1.6	Modern		
246207	HF-7	70	*Callianax baetica*	-737.6	0.7	10750	25	12195-11741
260448	HF-12	59	Bivalve	-798.1	0.6	12855	25	14787-14217
260447	HF-12	63	Bivalve	-852.7	0.6	15385	35	17967-17551
260446	HF-12	67	Shell fragment	-997.9	0.4	49700	1600	54911-48737
260445	HF-12	71	Gastropod	-993.8	0.4	40770	550	44014-42414

889

890 TABLE 1. CHS radiocarbon geochronology (modified from Medri et al., 2022). Ages marked by
891 an asterisk are out of sequence.

892

Lab Code	n[a]	CAM Over Dispersion[b]	CAM De[c] (Gray)	CAM Age[c] (ka)
HF-1(92-96cm)	15(29)	19%	11.8 ± 0.6	12.1 ± 0.7
HF-2(59-64cm)	14(28)	25%	2.67 ± 0.18	2.47 ± 0.18
HF-2(96-101cm)	14(35)	27%	13.1 ± 1.0	12.3 ± 1.0
HF-4(119-127cm)	10(15)	20%	7.75 ± 0.51	6.95 ± 0.48
HF-4(159-166cm)	10(15)	23%	14.7 ± 1.1	11.8 ± 0.9
HF-6(239-248cm)	6(10)	12%	8.88 ± 0.49	8.55 ± 0.50
HF-7(22-33cm)	18(25)	16%	11.7 ± 0.5	10.6 ± 0.5
HF-7(68-76cm)	19(30)	12%	14.9 ± 0.5	12.4 ± 0.4
HF-15(95-103cm)	26(32)	14%	21.9 ± 0.6	18.5 ± 0.6
HF-15(120-130cm)	5(20)	29%	119 ± 16	78.8 ± 10.9
HF-15(134-144cm)	11(16)	19%	111 ± 7	67.7 ± 4.2

TABLE 2. Table of Optical Stimulated Luminescence ages derived from core samples. First column denotes core and sample interval. The central age model (CAM) is used as this provides the closest agreement with radiocarbon ages (Table 1). See supplementary materials for additional details. [a]Number of aliquots meeting acceptance criteria, parentheses indicate total number of aliquots measured. [b] Defined as the statistical dispersion beyond what would be expected for a perfectly bleached sample (Galbraith and Roberts, 2012). [c] Determined using the function calc CentralDose from the R-Luminescence package. Uncertainty is 2 σ.

	Unit 1 (n = 7)		Unit 2 (n = 7)	
	Mean	S.D.	Mean	S.D.
Quartz	20.0	2.0	15.2	4.2
Polycrystalline Quartz	5.5	1.1	4.3	1.9
Plagioclase Feldspar	15.1	1.9	11.8	2.6
Sedimtary Lithic & Chert	39.0	5.2	30.1	2.9
Volcanic Lithic	6.4	1.1	3.9	1.1
Carbonate bioclast	5.3	2.5	31.9	10.0
Heavy Mineral	8.4	1.8	2.2	1.3
Mica	0.2	0.5	0.4	0.5
QmpFLt	30,18,53		30,18,52	

TABLE 3. Composition of fine-grained sand sampled from CHS cores. S.D. is standard deviation.

908 FIGURE CAPTIONS

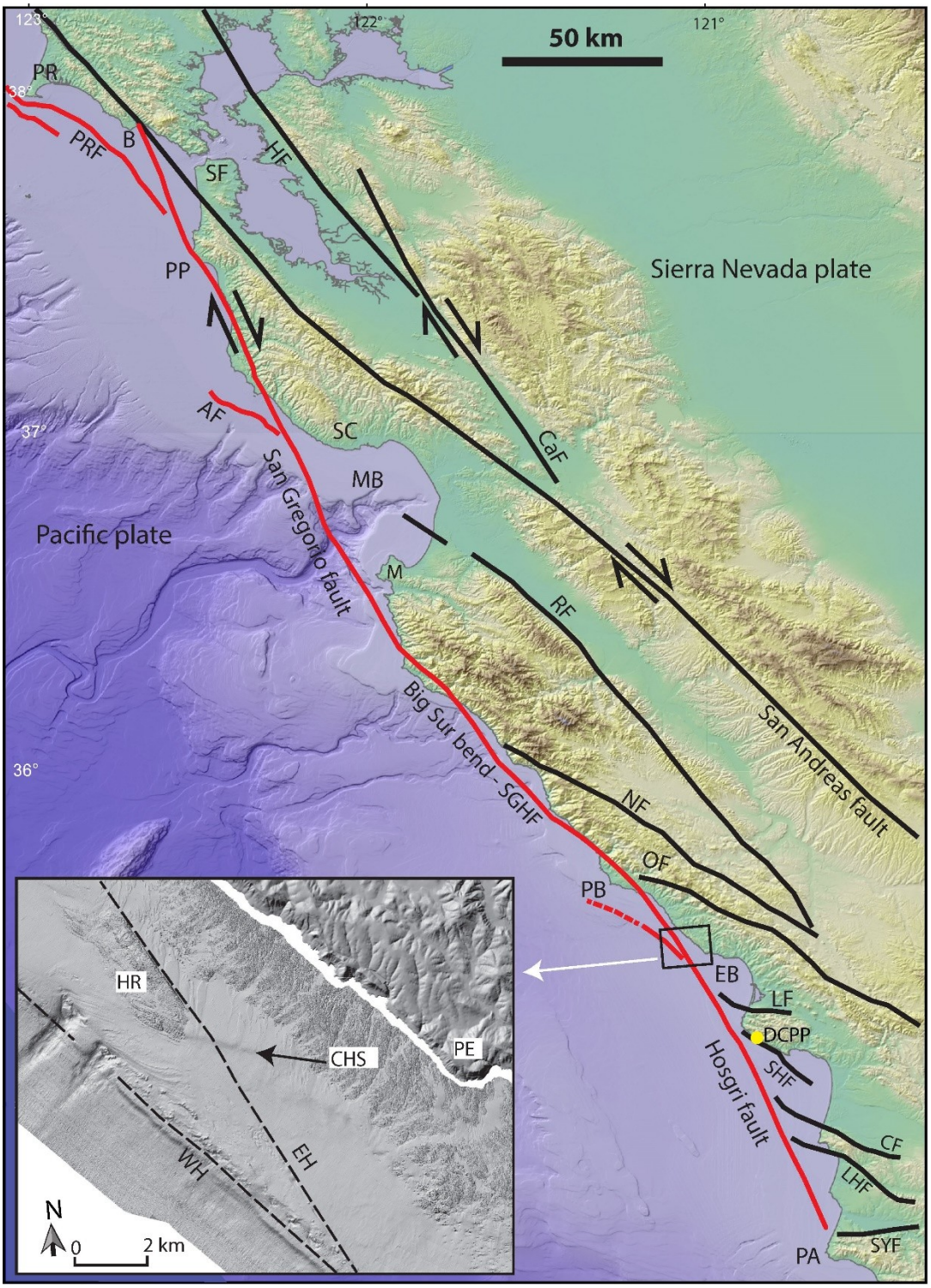

909

910 FIGURE 1. Regional map showing the main fault structures that are part of the Pacific-North

911 American Plate Boundary along central California. The San Gregorio-Hosgri Fault (SGHF)

system is predominantly located near the coastline and highlighted in red. Inset map shows the focus region of this study where the Cross Hosgri Slope (CHS) is located. AF = Ascension Fault; B = Bolinas; CaF= Calaveras Fault; CF = Casmalia Fault; DCPP = Diablo Canyon Power Plant: EB = Estero Bay; EH = Eastern strand of Hosgri Fault; HF = Hayward Fault; HR = Hosgri ridge; LF = Los Osos Fault; LHF = Lions Head Fault; M = Monterey; MB = Monterey Bay; NF = Nacimiento Fault; OF = Oceanic Fault; PA = Point Arguello; PB = Piedras Blancas; PE = Point Estero; PP = Pillar Point; PR = Point Reyes; PRF = Point Reyes Fault; RF = Rinconada Fault; SC = Santa Cruz; SF = San Francisco; SHF = Shoreline Fault; SYF = Santa Ynez Fault; WH = Western strand of Hosgri Fault.

935

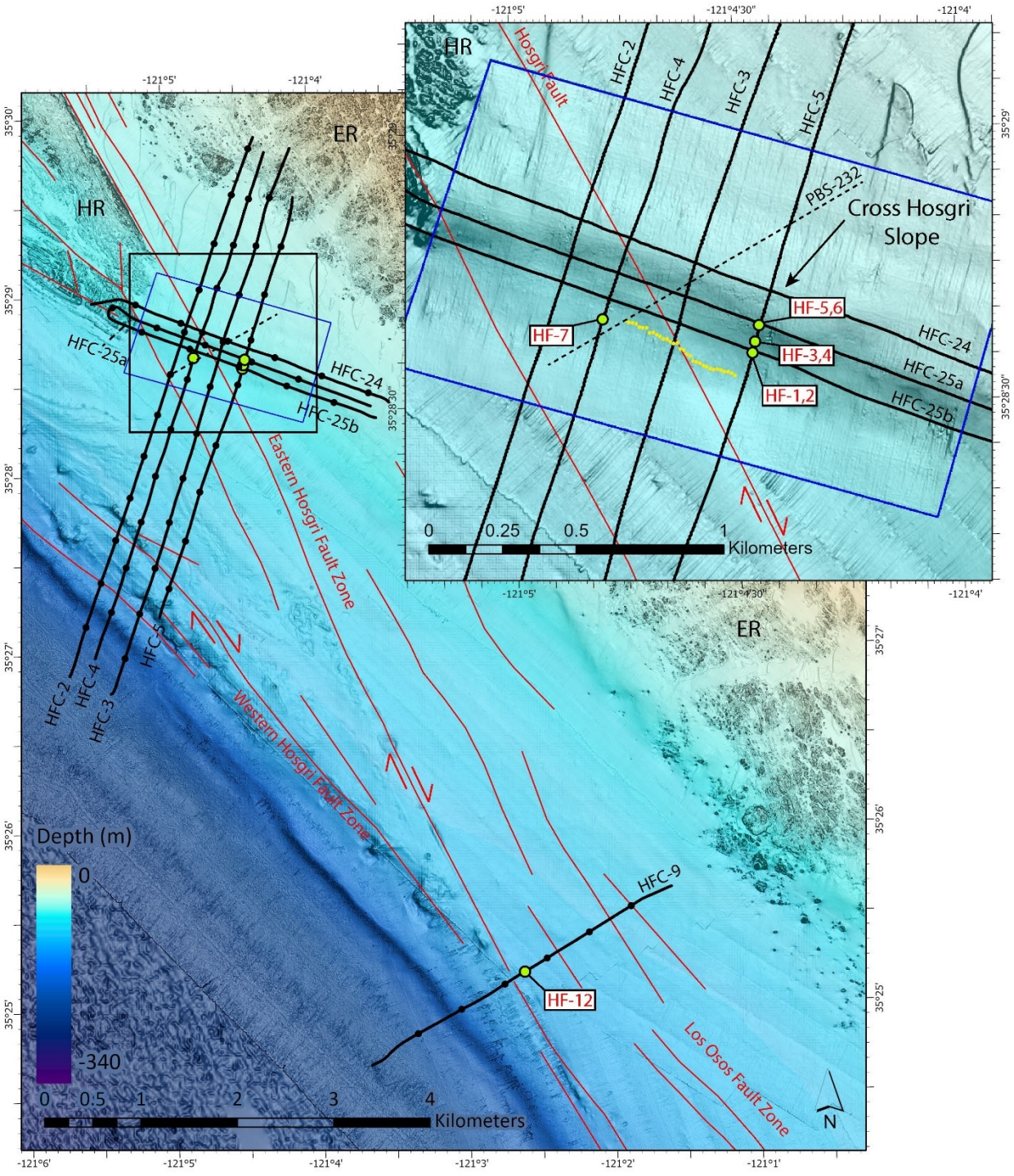

936

937 FIGURE 2. Map showing high resolution bathymetry and locations of CHIRP tracklines (black)

938 and sediment cores (green) in the study region. Inset shows details of CHIRP tracklines and core

locations along the Cross Hosgri Slope (CHS). Inset location outlined with black rectangle. Red lines denote fault locations from the USGS Quaternary Fault and Fold database (Walton et al., 2020). Black circles along the CHIRP tracklines denote every 500 shots. Blue polygon outlines USGS collected Reson 7111 multibeam bathymetry (Hartwell et al., 2013) and yellow points denote lower slope break points used for slip rate analysis in Johnson et al. (2014). Additional bathymetry source includes data from the California Seafloor Mapping Program (Johnson et al., 2017). Dashed black line shows location of sparker profile used in Johnson et al., 2014 and shown in Figure 11. ER = Estero Rocks, HR = Hosgri Ridge.

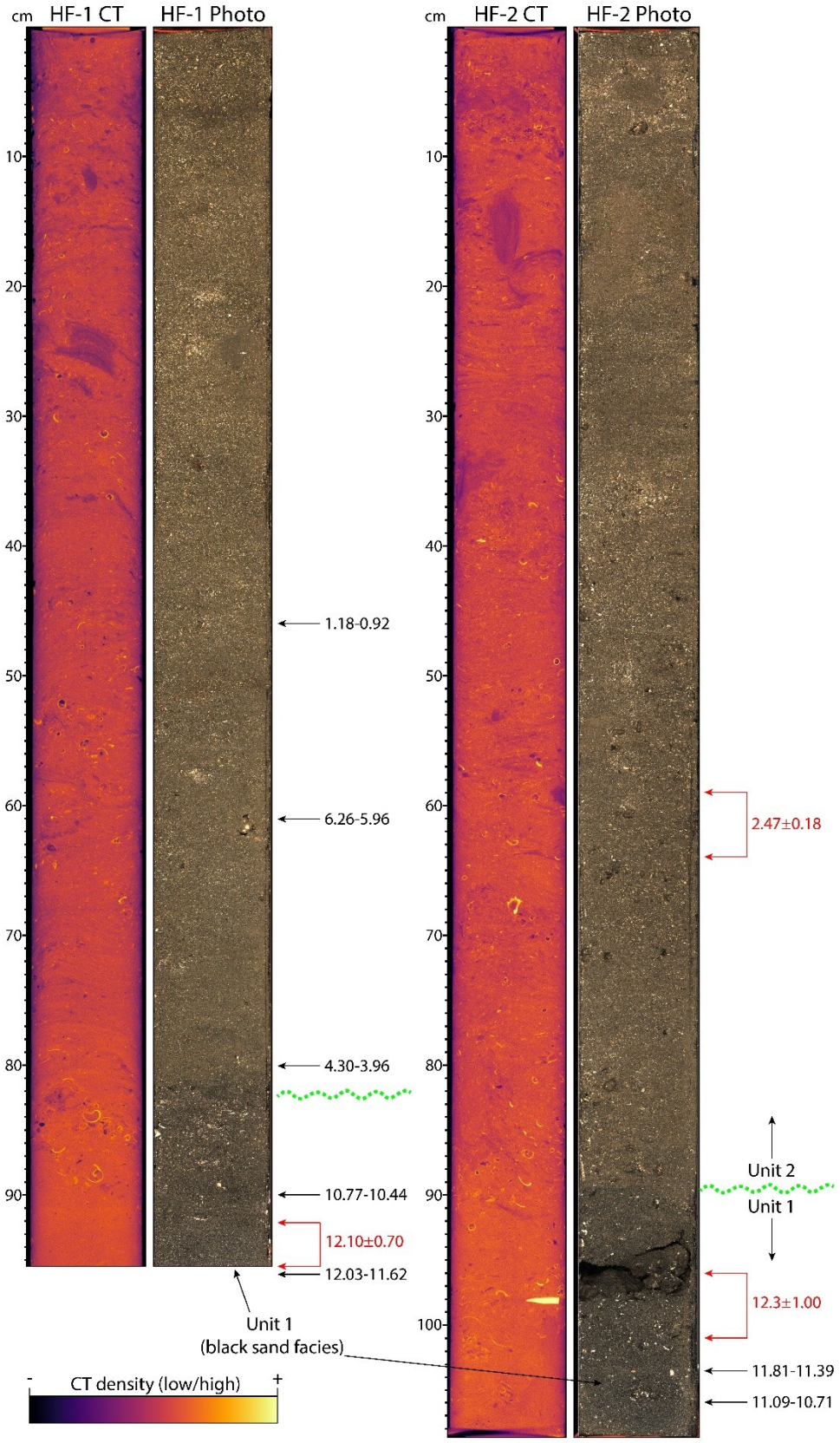
cm
HF-1 CT
HF-1 Photo
cm
HF-2 CT
HF-2 Photo
10
20
30
40
50
60
70
80
90
100
1.18-0.92
6.26-5.96
4.30-3.96
10.77-10.44
12.10±0.70
12.03-11.62
Unit 1
(black sand facies)
2.47±0.18
Unit 2
Unit 1
12.3±1.00
11.81-11.39
11.09-10.71
-
CT density (low/high)
+

FIGURE 3. CT scan and photos of sediment cores HF-1 and HF-2. Radiocarbon ages are noted in black, whereas OSL ages are provided in red. Wavy dashed green line denotes the transition zone from Unit 1 below to Unit 2 above. Ages are shown in ka.

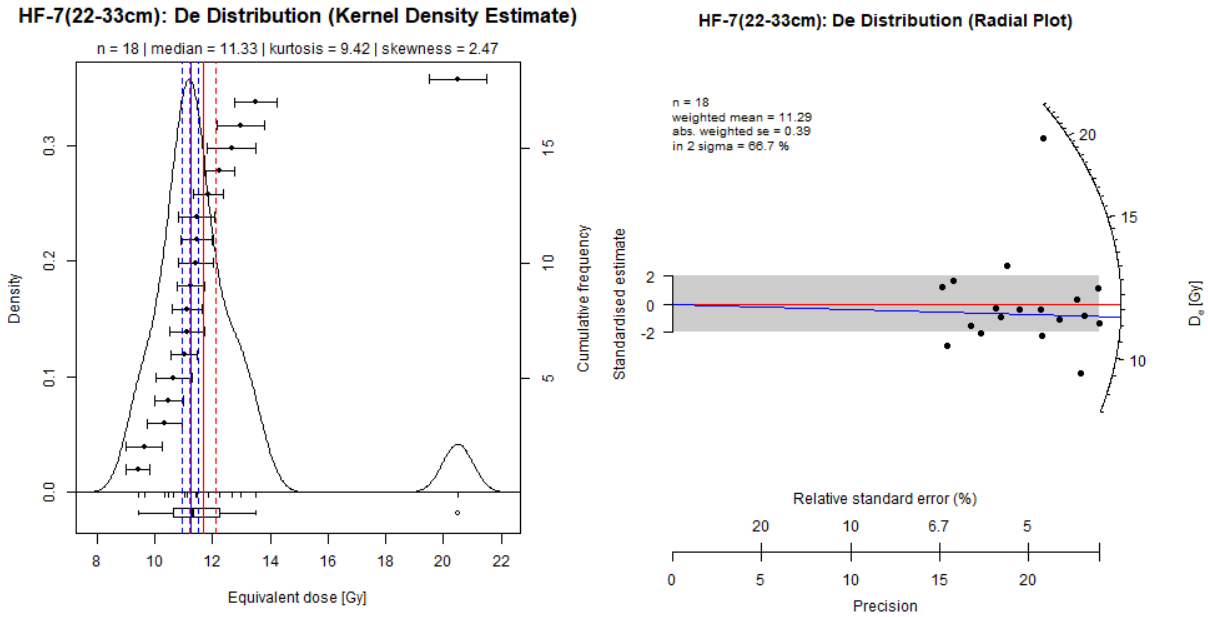

FIGURE 4. Plots of Equivalent Dose for HF-7(22-33cm). Red lines show CAM (Central Age Model) equivalent dose, blue lines show MAM (Minimum Age Model) equivalent dose, solid line shows the age, and dashed lines show uncertainty. We analyzed HF-7 (22-33cm) using Quartz OSL on 125-150 µm size grains. Out of 25 aliquots, 18 produced acceptable luminescence characteristics and passed acceptance criteria (Supplementary Material). Aliquots that passed acceptance criteria are plotted as a kernel density estimate (left) and as a radial plot (right).

978

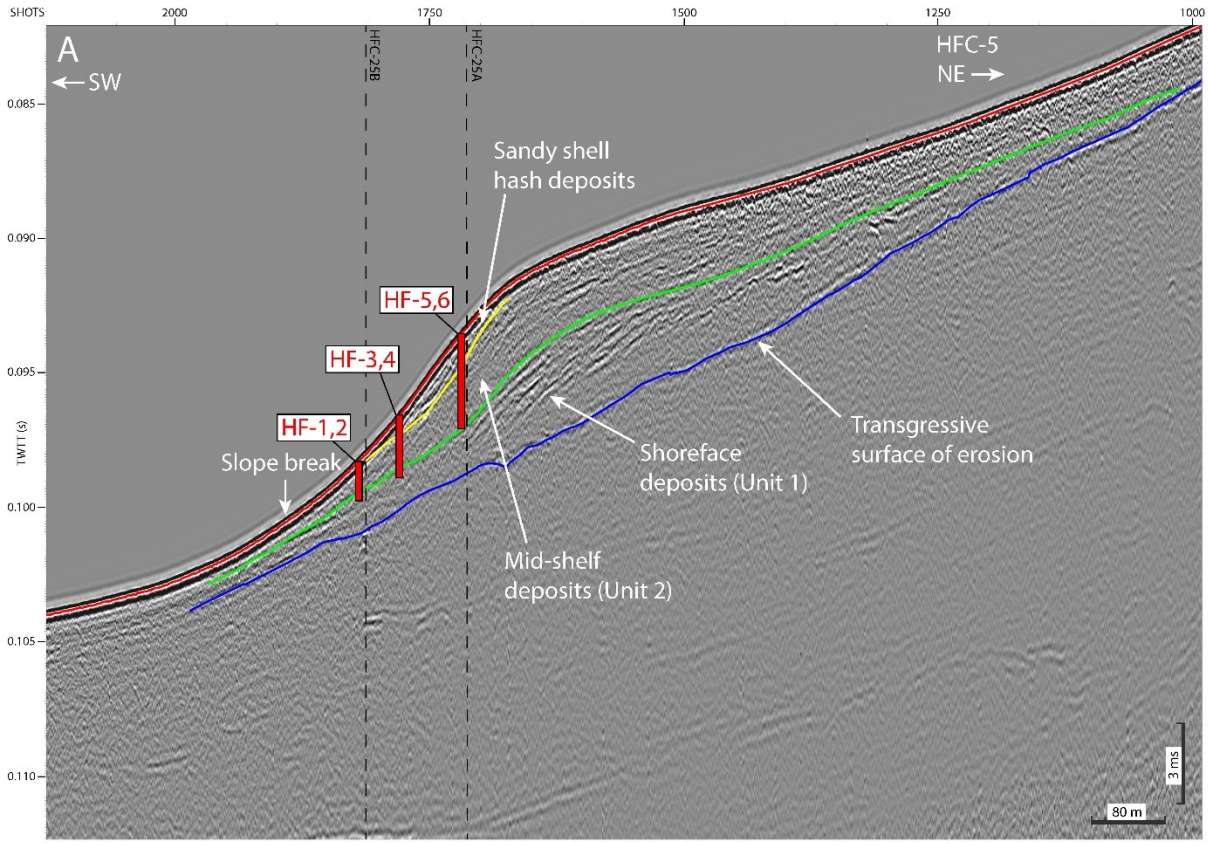
SHOTS
2000
1750
1500
1250
1000
A
SW
HFC-25B
HFC-25A
HFC-5
NE
Sandy shell
hash deposits
HF-5,6
HF-3,4
HF-1,2
Slope break
Shoreface
deposits (Unit 1)
Transgressive
surface of erosion
Mid-shelf
deposits (Unit 2)
TWTT (s)
0.085
0.090
0.095
0.100
0.105
0.110
3 ms
80 m

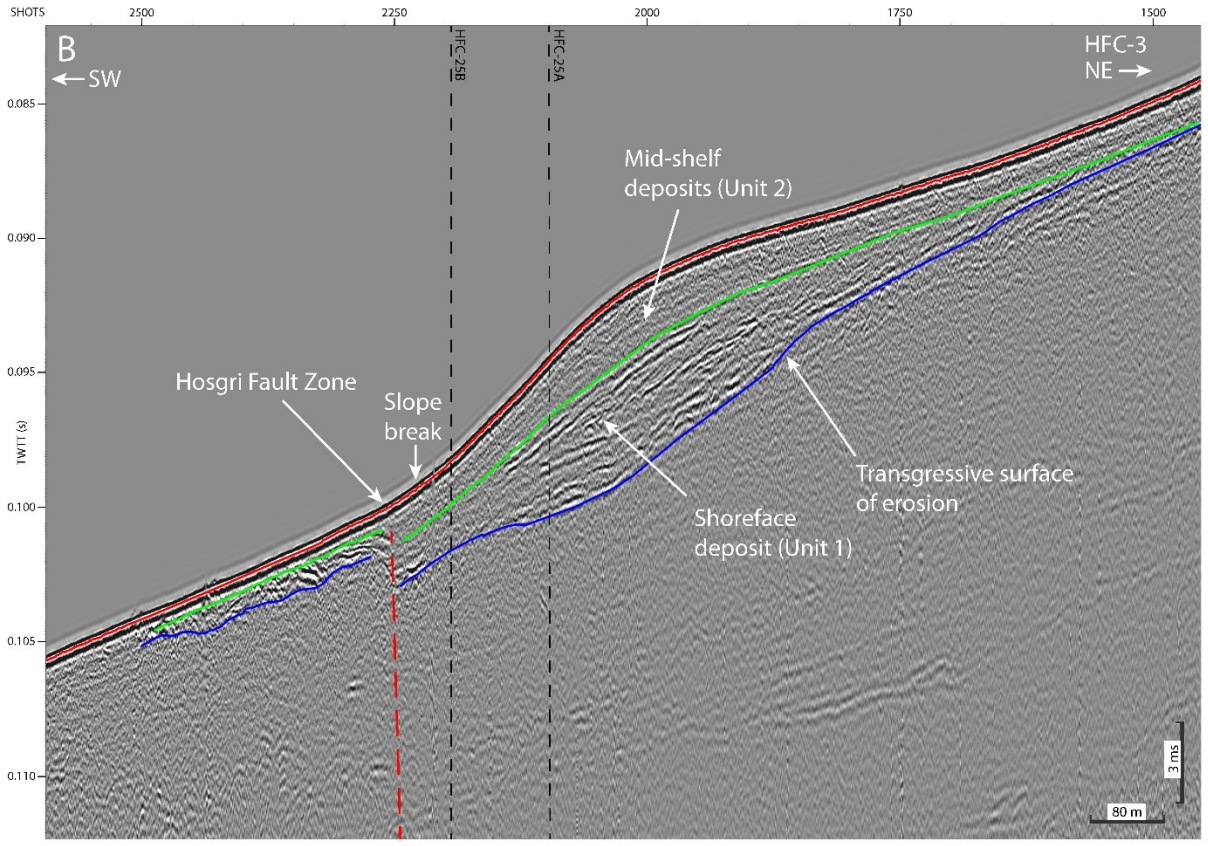
SHOTS
2500
2250
2000
1750
1500
B
SW
HFC-25B
HFC-25A
HFC-3
NE
Mid-shelf
deposits (Unit 2)
Hosgri Fault Zone
Slope
break
Transgressive surface
of erosion
Shoreface
deposit (Unit 1)
TWTT (s)
0.085
0.090
0.095
0.100
0.105
0.110
3 ms
80 m

979

F

IGURE 5. CHIRP profiles across the CHS. (A) CHIRP profile HFC-5 that crosses core sites HF-1 through HF-6. (B) CHIRP profile HFC-3 showing offset transgressive surface of erosion on Unit 1 near the toe of the CHS. Blue horizon denotes the transgressive surface of erosion, the green horizon traces the top of paleo shoreface deposits (Unit 1), the yellow horizon traces the bottom of the sandy shell hash deposits, and the seafloor is delineated in red. Core locations are shown in red, and the Hosgri Fault Zone is marked with a dashed red line on panel B. Vertical dashed black lines show location of crossing CHIRP profiles HFC-25a and HFC-25b

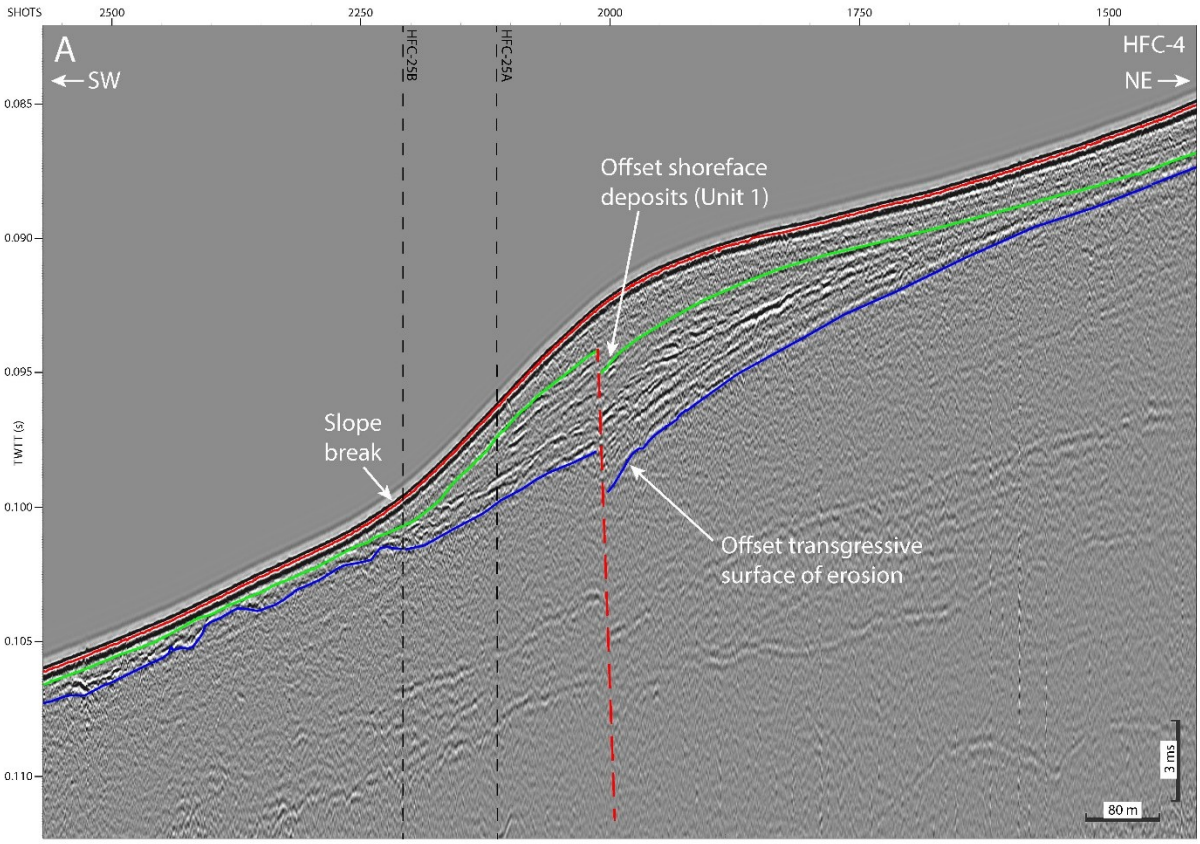
SHOTS
2500
2250
2000
1750
1500
A
SW
HFC-25B
HFC-25A
HFC-4
NE
Offset shoreface
deposits (Unit 1)
Slope
break
Offset transgressive
surface of erosion
TWTT (s)
0.085
0.090
0.095
0.100
0.105
0.110
3 ms
80 m

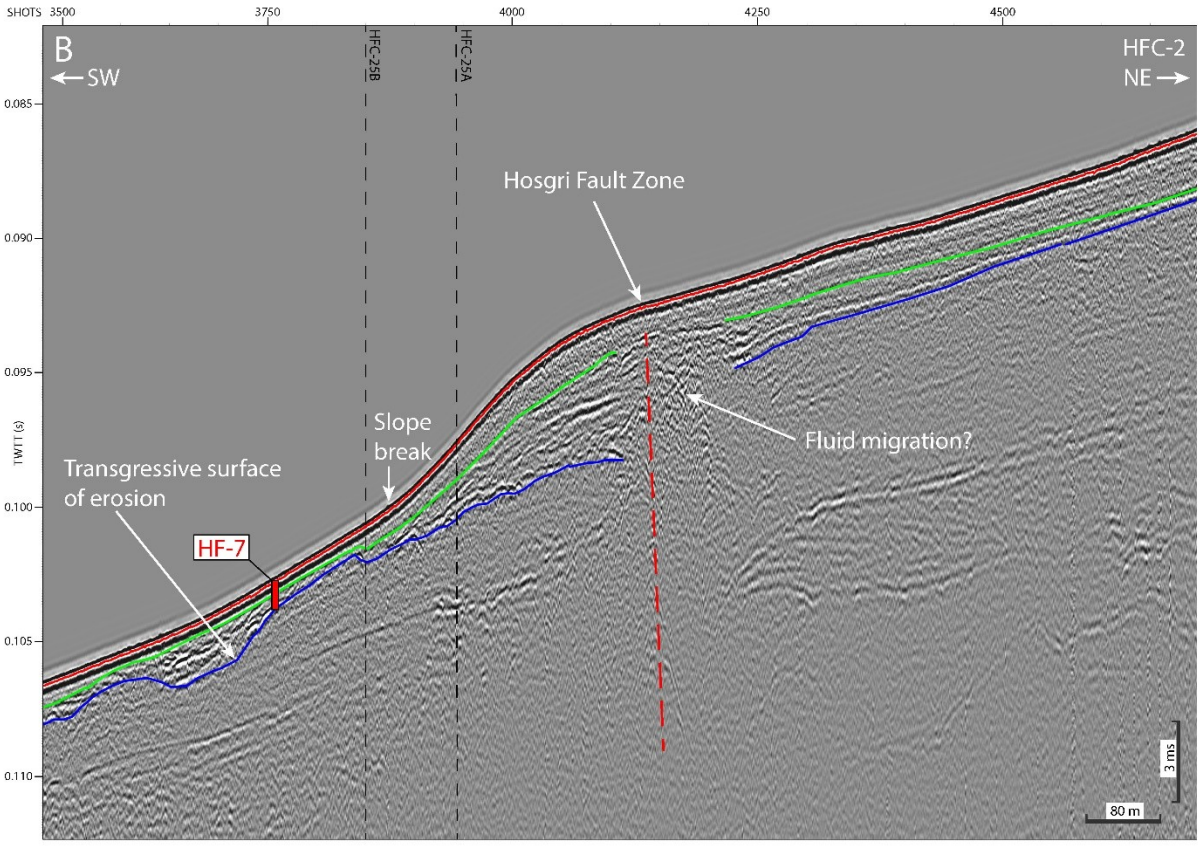
SHOTS
3500
3750
4000
4250
4500
B
SW
HFC-25B
HFC-25A
HFC-2
NE
Hosgri Fault Zone
Slope
break
Fluid migration?
Transgressive surface
of erosion
HF-7
TWTT (s)
0.085
0.090
0.095
0.100
0.105
0.110
3 ms
80 m

FIGURE 6. CHIRP profiles across the CHS. (A) CHIRP profile HFC-4 that shows clear offset of the transgressive surface of erosion and paleo shoreface deposits. (B) CHIRP profile HFC-2 that crosses the Hosgri Fault along the upper portion of the CHS. Blue horizon denotes the transgressive surface of erosion, the green horizon traces the top of paleo shoreface deposits (Unit 1). HF-7 core location is shown in red, and the Hosgri Fault is marked with a dashed red line. Vertical dashed black lines show location of crossing CHIRP profiles HFC-25a and HFC-25b.

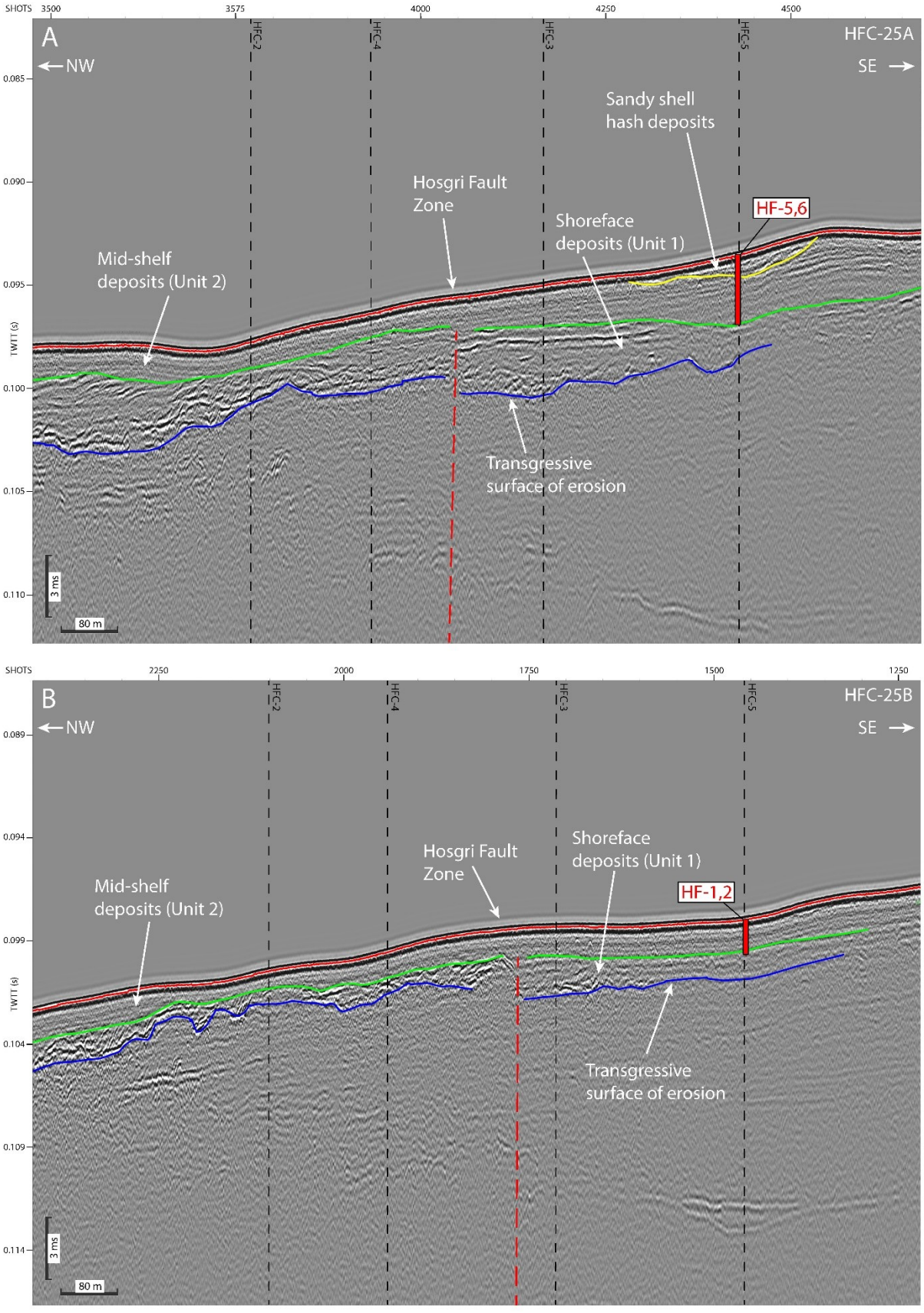
SHOTS 3500
3575
4000
4250
4500
A
NW
SE
HFC-25A
HFC-2
HFC-4
HFC-3
HFC-5
Sandy shell hash deposits
Hosgri Fault Zone
Shoreface deposits (Unit 1)
HF-5,6
Mid-shelf deposits (Unit 2)
Transgressive surface of erosion
TWTT (s)
0.085
0.090
0.095
0.100
0.105
0.110
3 ms
80 m
SHOTS 2250
2000
1750
1500
1250
B
NW
SE
HFC-25B
HFC-2
HFC-4
HFC-3
HFC-5
Hosgri Fault Zone
Shoreface deposits (Unit 1)
HF-1,2
Mid-shelf deposits (Unit 2)
Transgressive surface of erosion
TWTT (s)
0.089
0.094
0.099
0.104
0.109
0.114
3 ms
80 m

FIGURE 7. Along slope CHIRP profiles across the CHS. (A) CHIRP profile HFC-25a that transects the middle portion of the CHS. (B) CHIRP profile HFC-25b that transects the lower portion of the CHS. Blue horizon denotes the transgressive surface of erosion, the green horizon traces the top of paleo shoreface deposits (Unit 1), and the yellow horizon traces the base of the sandy shell hash deposits. Core locations are shown in red, and the Hosgri Fault is marked with a dashed red line. Vertical dashed black lines show location of crossing CHIRP profiles HFC-2, HFC-3, HFC-4, and HFC-5.

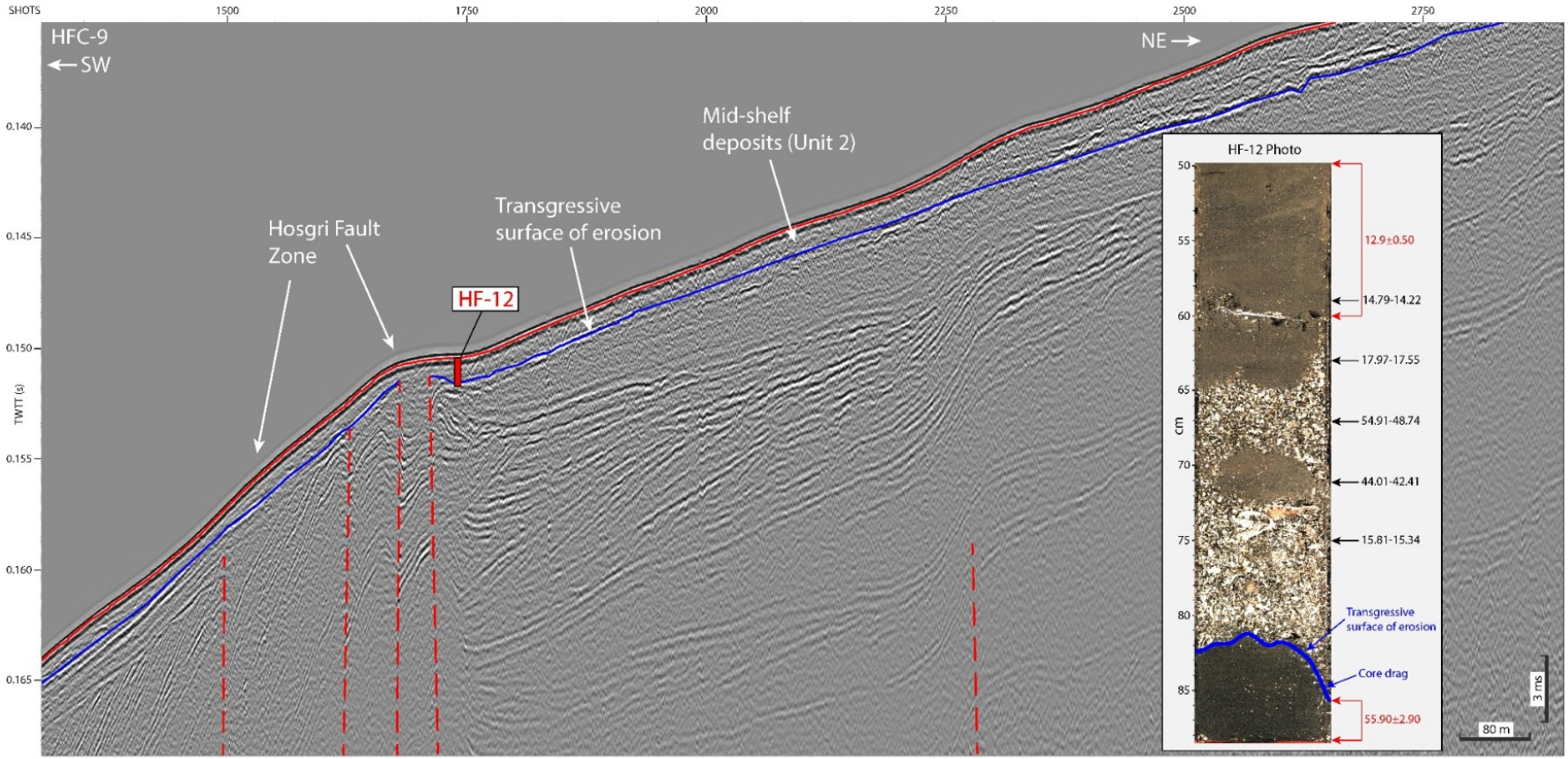
SHOTS
1500
1750
2000
2250
2500
2750
HFC-9
← SW
NE →
Mid-shelf
deposits (Unit 2)
Transgressive
surface of erosion
Hosgri Fault
Zone
HF-12
TWTT (s)
0.140
0.145
0.150
0.155
0.160
0.165
HF-12 Photo
cm
50
55
60
65
70
75
80
85
12.9±0.50
14.79-14.22
17.97-17.55
54.91-48.74
44.01-42.41
15.81-15.34
Transgressive
surface of erosion
Core drag
55.90±2.90
3 ms
80 m

FIGURE 8. CHIRP profile HFC-9 located south the CHS. Profile crosses the mid-shelf region and images the extensive trangressive surface of erosion unconformity also seen below the CHS. Sediment core HF-12 is located along the profile on the flank of the Hosgri Fault Zone. Inset shows the bottom portion of HF-12 and the associated radiocarbon and OSL ages. Note the jump in ages above and below the blue horizon. Radiocarbon ages are noted in black, whereas OSL ages are provided in red.

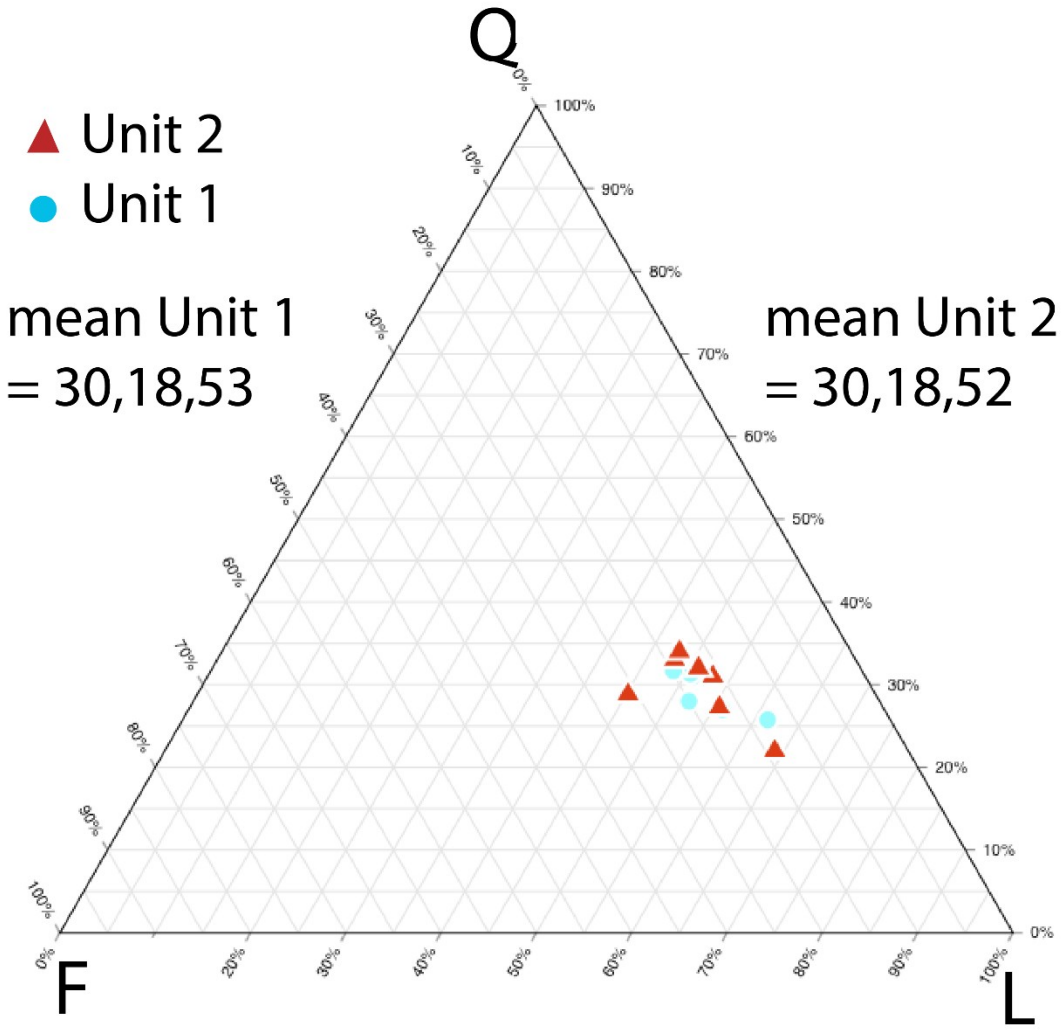

FIGURE 9. Tenrary plot showin CHS sand composition. Q = monocrystalline and polycrystalline quartz; L = siliciclastic lithic fragments, chert, and volcanic lithic fragments.

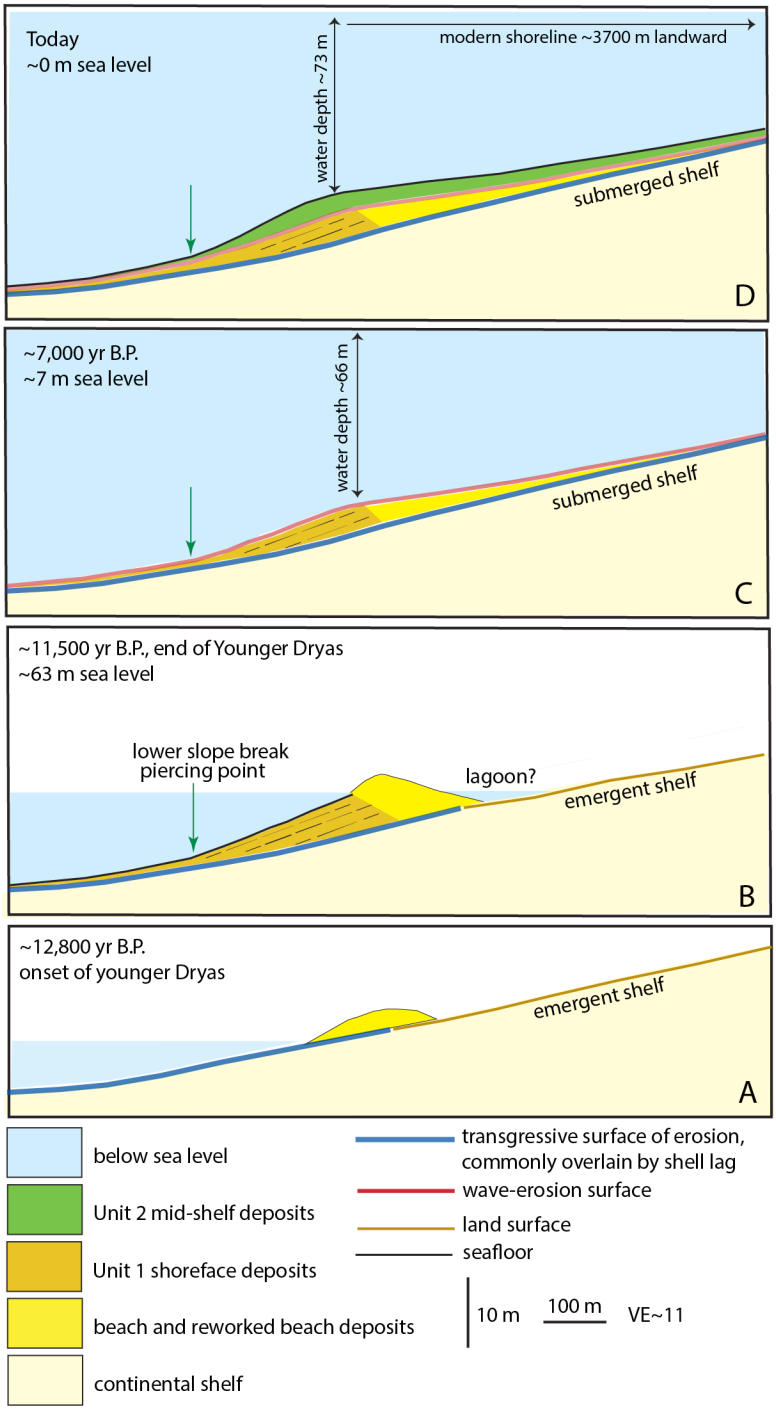

FIGURE 10. CHS depositional model. See text for discussion.

1088

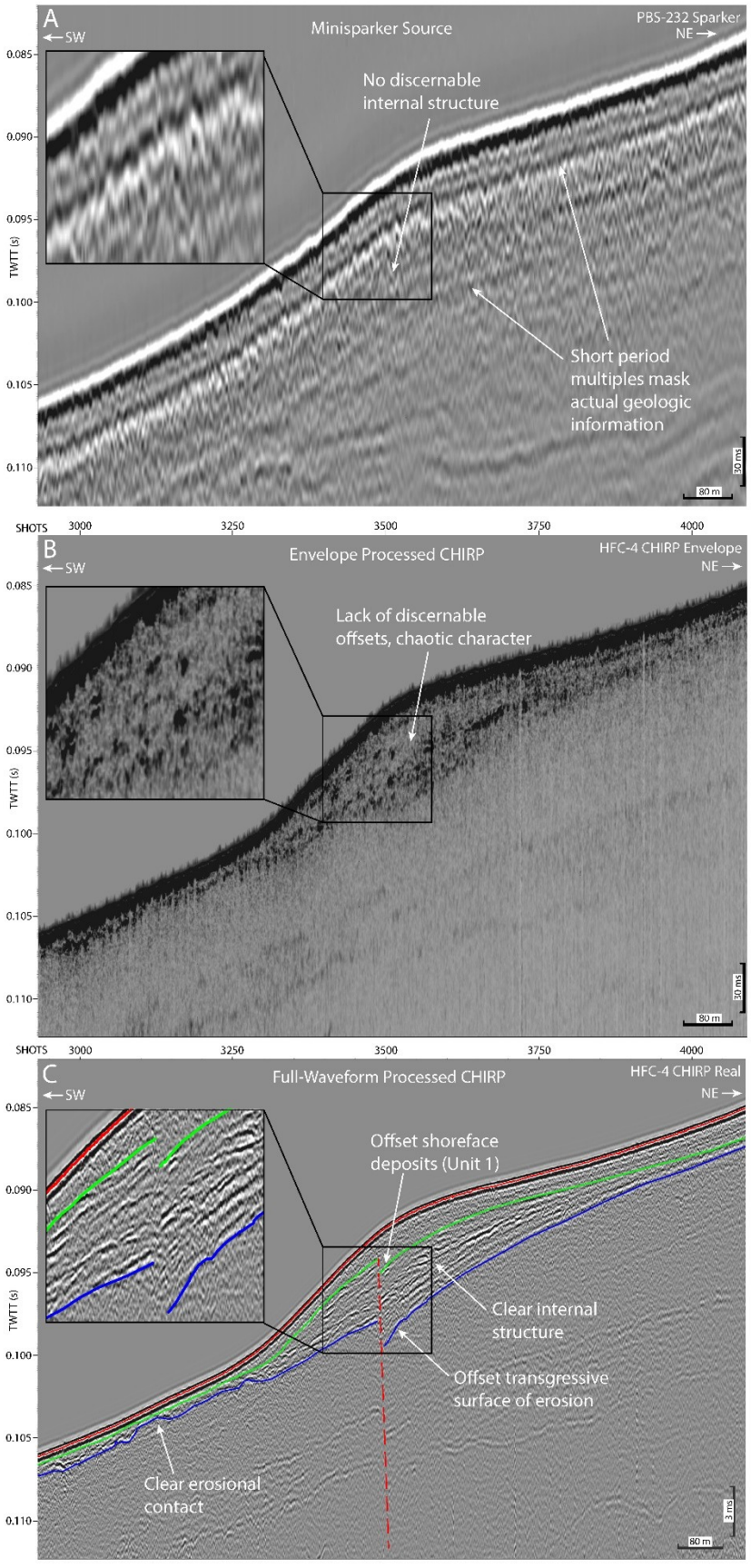
A
SW
Minisparker Source
PBS-232 Sparker
NE
No discernable
internal structure
Short period
multiples mask
actual geologic
information
TWT (s)
0.085
0.090
0.095
0.100
0.105
0.110
80 m
SHOTS
3000
3250
3500
3750
4000
B
SW
Envelope Processed CHIRP
HFC-4 CHIRP Envelope
NE
Lack of discernable
offsets, chaotic character
C
SW
Full-Waveform Processed CHIRP
HFC-4 CHIRP Real
NE
Offset shoreface
deposits (Unit 1)
Clear internal
structure
Offset transgressive
surface of erosion
Clear erosional
contact
3 ms

FIGURE 11. Three panels showing the differences of resolution and geologic resolvability for sparker and chirp data collected across the CHS. (A) Sparker profile PBS-232 collected across the CHS and shown in Johnson et al., 2014. (B) CHIRP profile HFC-4 shown in envelope with 1-pass swell correction. (C) CHIRP profile HFC-4 processed using the full waveform data and multiple swell correction steps. Note the jump is resolution from sparker to envelope CHIRP, and further improvement with full waveform (real) CHIRP data. Insets show 200% zoomed in portions of the profile with locations delineated by the black rectangles. See Figure 2 for locations of profiles.